

Kerr-Newman Black Holes in Weyl-Cartan Theory: Shadows and EHT constraints

Khadije Jafarzade^{1,2,3*}, Seyed Hossein Hendi^{1,2,4*†} Mubasher Jamil^{5,4‡}, and Sebastian Bahamonde^{6§}

¹*Department of Physics, School of Science, Shiraz University, Shiraz 71454, Iran*

²*Biruni Observatory, School of Science, Shiraz University, Shiraz 71454, Iran*

³*ICRANet-Mazandaran, University of Mazandaran, P. O. Box 47415-416, Babolsar, Iran*

⁴*Canadian Quantum Research Center 204-3002 32 Ave Vernon, BC V1T 2L7 Canada*

⁵*School of Natural Sciences, National University of Sciences and Technology, H-12, Islamabad 44000, Pakistan*

⁶*Department of Physics, Tokyo Institute of Technology 1-12-1 Ookayama, Meguro-ku, Tokyo 152-8551, Japan*

With the recent release of the black hole image of Sgr A* alongside the earlier image of M87*, one can achieve an in-depth understanding of gravitational physics at the horizon scale. According to the Event Horizon Telescope (EHT) collaboration, the observed image is consistent with the expected appearance of a Kerr black hole. In the present work, we consider Kerr-New black holes in Weyl-Cartan theory as a supermassive black hole (BH) and evaluate the parameters of the model with shadow size estimates done by the observations of M87* and Sgr A* from EHT. Such a study can be a possible way to distinguish Weyl-Cartan theory from general relativity and ensure the validity of the idea. Besides, we calculate the energy emission rate for the corresponding BH and discuss how the model's parameters affect the emission of particles around the black hole. With this investigation, we are able to examine the time evolution and lifetime of the black hole in such a theory of gravity.

I. INTRODUCTION

Black holes are the most fascinating predictions of general relativity which hold the key to answer several unresolved problems in theoretical physics including the nature of quantum gravity and the information loss paradox. For several decades after their prediction, the existence of black holes in the physical universe remained a mystery. However, two of the most remarkable predictions of Einstein's general theory of relativity namely, the black hole shadows and gravitational waves generated by black hole-black hole merger have been verified successfully in recent years. The LIGO-VIRGO collaboration detected gravitational wave signals produced by the merger of two black holes at high redshift, which has opened a new window of gravitational wave astronomy [1]. Remarkably, the Event Horizon Telescope has witnessed the formation of photon rings, which constitute the shadow, in the vicinity of the supermassive black hole in M87 galaxy and also Sgr A* supermassive black hole at the heart of Milky Way galaxy, for the first time [2]. For M87* supermassive black hole, the EHT team has detected large scale magnetic fields and plasma near the black hole using polarized synchrotron radiation [3]. In addition, the EHT team inferred a mass accretion rate onto the black hole in M87 of $(3 - 20) \times 10^{-4}$ solar mass per year. Thus, the M87 central black hole is an active black hole associated with an accretion disk and a jet.

The existence of photon rings around these supermassive black holes suggests the existence of accretion disks constituting high energy particles in motion and eventually falling into the black hole. Some of the photons emitted from the accretion disk with specific critical energy can move in circular orbits near the black hole. Due to chaotic motions and collisions between particles, these photons can escape towards an external observer. The paths followed by the photons in circular motion and during their escape can help us identify the spacetime curvature in strong gravity regime. Inside the bright rings, there lies a black region which is termed the black hole shadow whose geometry, radius and angular diameter size can be helpful to constrain the black hole candidate models from different gravitational theories. Eventually, we want to understand if the observed black holes possess any spin, charge, scalar hair or any deformations that are compatible with our existing gravitational theories. Further, the same observations would be instructive to differentiate the general relativity and the alternative extended models of gravity and eventually rule out some of the existing gravity theories. In literature, the black hole shadows are modelled and constrained not only using black hole candidates but wormhole and naked singularity spacetimes as well [4]. Since a small size black hole (such as Sgr A*) produces a higher spacetime curvature as compared to large size black hole (such as M87*), therefore observations of shadow of Sgr A* can impose stringent constraints on the free parameters of black hole spacetime candidates, for a detailed review on available constraints on black holes in general relativity and modified gravity, see

* email address: khadije.jafarzade@gmail.com

† email address: hendi@shirazu.ac.ir (corresponding author)

‡ email address: mjamil@sns.nust.edu.pk (corresponding author)

§ email address: sbahamondebeltran@gmail.com

[5–13].

The most natural family of black hole candidates to test and analyze the black hole shadows is the Kerr black hole and other spinning black holes with free parameters derived by solving the governing field equations of modified gravity theories. Separate investigations have been reported in the literature over the past several years to constrain black hole candidates in extended gravity theories using shadows. Some of these theories include Horava Lifshitz, Einstein-Aether, Gauss-Bonnet, massive gravity, generalized teleparallel, Einstein-Maxwell-Dilaton, Chern-Simons, Einstein-Yang-Mills, string theory, and loop quantum gravity inspired black holes (see references [14]). In this article, we intend to investigate constraints on the newly proposed Weyl-Cartan theory (WCT) spinning black holes using the EHT data.

WCT, a theoretical framework that extends general relativity by incorporating non-metricity and torsion, offers intriguing prospects in the study of black hole physics [15–18]. In other words, all three geometric properties—curvature, torsion, and non-metricity—are nonzero in this theory of gravity and they are fixed dynamically by their equations of motion. Unlike other approaches, such as Einstein-Cartan theory [19–22] or teleparallel gravity [23–26], WCT allows for a more comprehensive description of the gravitational field by considering both the metric tensor and additional geometric quantities. Then, torsion is sourced by intrinsic spin and non-metricity by intrinsic dilations and shears. This inclusion of non-metricity and torsion enables a richer understanding of the dynamics near black holes, particularly in extreme conditions where spacetime curvature is significant. By accounting for these additional geometric properties, WCT provides a more nuanced depiction of the gravitational interaction, potentially offering insights into phenomena such as the behavior of matter and energy within the event horizon, the formation and evolution of black holes, and the resolution of long-standing puzzles like the information paradox. While further research and empirical validation are necessary to fully assess the merits of WCT in black hole physics, its unique approach holds promise for advancing our comprehension of these enigmatic cosmic entities. Moreover, it is expected that the intrinsic properties of matter (spin, dilations, and shears) might be relevant in strong gravity regimes, and then, supermassive black holes could in principle be endowed with those intrinsic properties.

This paper is organized as follows: In Sec. II, we briefly describe the geometrical features of charged rotating black holes in WCT. In Sec. III A, we study the effect of the parameters of the model on null geodesics, which in turn affect the photon sphere radius and shadow radii. In Sec. III B, we examine energy emission rate and the influence of the WC parameters on the emission of particles. The black hole shadow observables and their applications in estimating the WC parameters are presented in Sec. IV. Moreover, constraints on the parameters of the model are deduced using the M87* and Sgr A* black hole shadow observational data for the inclination angles of 17° and 50°. The paper is finally concluded with some closing remarks.

II. ROTATING BHs IN WEYL-CARTAN THEORY

WCT is formulated as a gauge theory of gravity where the field strengths tensors are related to the curvature tensor $\tilde{R}^\lambda_{\mu\nu\beta}$, the torsion tensor which is the antisymmetric part of the connection $T^\lambda_{\mu\nu} = 2\tilde{\Gamma}_{[\mu\nu]}$, and the non-metricity tensor $Q_{\lambda\mu\nu} = \tilde{\nabla}_\lambda g_{\mu\nu}$. Then, in this framework, the affine connection is no longer the Levi-Civita and provides new degrees of freedom that are independent of the metric (see [17] for a review on this topic).

In this work, we are interested in a particular theory within WCT that has been constructed and studied in a series of papers [27–32]. This theory is constructed from gauge invariants in a way that when torsion and non-metricity are vanishing, the resulting theory gives the Einstein's field equations. Further, this theory is constructed from field strength tensors coming from the generalized Bianchi identities that introduce dynamics in both torsion and non-metricity. A new rotating black hole solution with dynamical torsion and nonmetricity fields has been found in [31], and the resulting spacetime metric is given by

$$\begin{aligned} ds^2 = & - \left(\Psi(r, \theta) - \frac{1}{3} \frac{a^4 \Lambda \cos^2 \theta \sin^2 \theta}{r^2 + a^2 \cos^2 \theta} \right) dt^2 + \frac{r^2 + a^2 \cos^2 \theta}{(r^2 + a^2 \cos^2 \theta) \Psi(r, \theta) + a^2 \sin^2 \theta} dr^2 + \frac{r^2 + a^2 \cos^2 \theta}{1 + \frac{1}{3} a^2 \Lambda \cos^2 \theta} d\theta^2 \\ & + \sin^2 \theta \left[r^2 + a^2 + a^2 (1 - \Psi(r, \theta)) \sin^2 \theta + \frac{a^2 \Lambda \cos^2 \theta (r^2 + a^2)^2}{3 (r^2 + a^2 \cos^2 \theta)} \right] d\varphi^2 \\ & - 2a \sin^2 \theta \left[1 - \Psi(r, \theta) + \frac{a^2 \Lambda (r^2 + a^2) \cos^2 \theta}{3 (r^2 + a^2 \cos^2 \theta)} \right] dt d\varphi, \end{aligned} \quad (2.1)$$

with

$$\Psi(r, \theta) = 1 - \left\{ 2Mr - [q_e^2 + q_m^2 + d_1 k_s^2 - 4e_1(k_e^2 + k_m^2)] + \frac{1}{3} \Lambda r^2 (r^2 + a^2) \right\} / (r^2 + a^2 \cos^2 \theta), \quad (2.2)$$

where the quantity M is the mass parameter and a is the rotation parameter. q_e and q_m are related to the electric and magnetic charges, respectively. k_s represents the intrinsic spin charge. The integration constants k_e and k_m are, respectively, the electric and magnetic intrinsic dilation charges. Metric (2.1) describes a Kerr-Newman Weyl-Cartan geometry connected to the electric and magnetic dilation charges related to the nonmetricity tensor, as well as by a spin charge related to the torsion tensor. Note that the theory producing the above solution is part of WCT with the traceless part of non-metricity being zero. Then, the shear charge is absent. From a phenomenological perspective, such a solution can represent the asymptotic gravitational field of a rotating black hole in a Weyl-Cartan regime with scale invariance [28], whose spin charge is much smaller than the external rotation, or vice versa ($|ak_s| \ll 1$). In fact, this condition characterizes the decoupling limit between the orbital and the spin angular momentum of the solution.

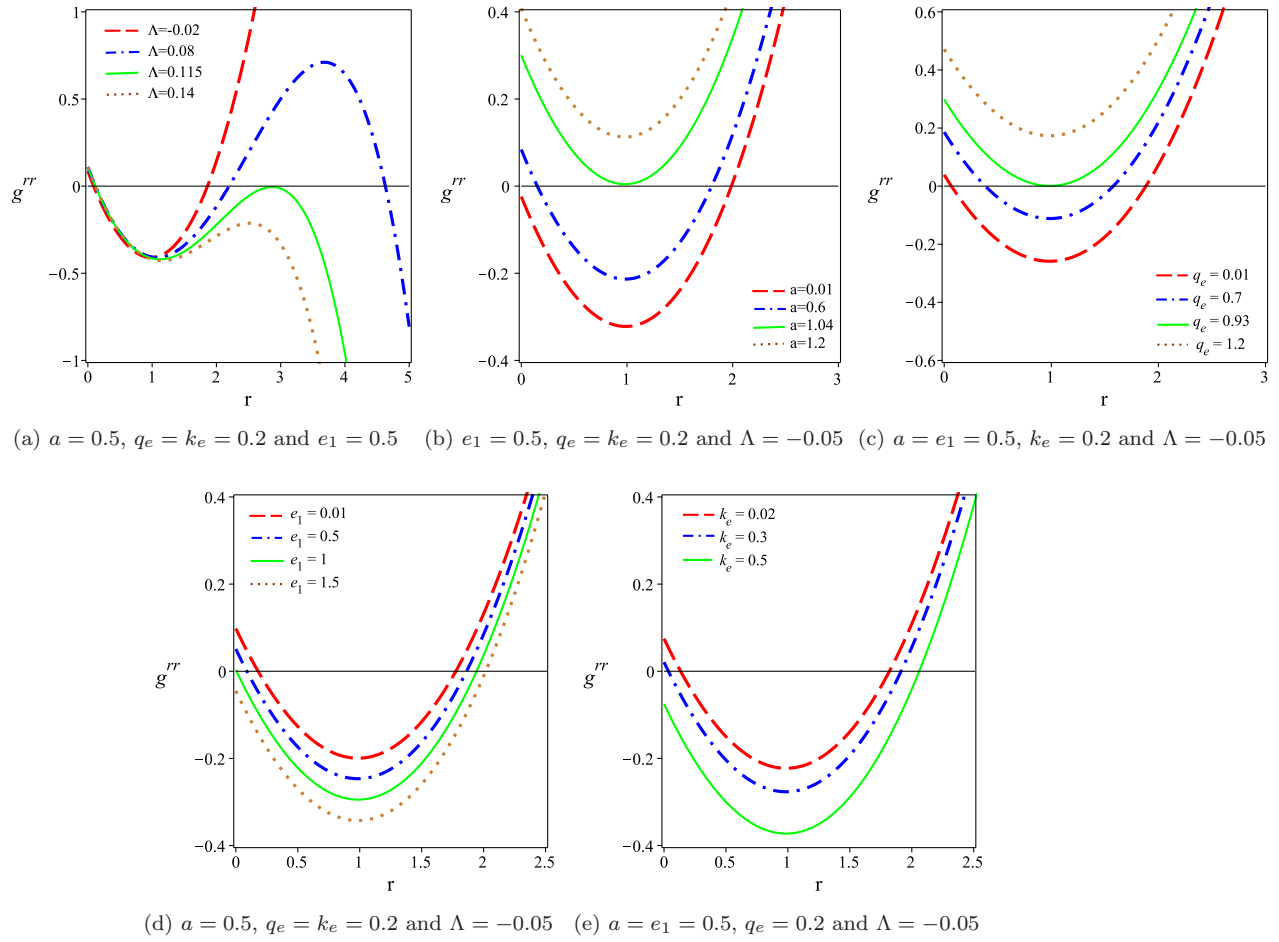


FIG. 1: The function g^{rr} versus r for $k_s = 10^{-6}$, $q_m = k_m = 0.2$, $d_1 = 0.5$ and $M = 1$.

It is worthwhile to investigate the geometrical structure and physical properties of this solution. A singular solution could be interpreted as a black hole solution if two conditions are satisfied: I) The existence of a non-removable singularity. II) Presence of at least one event horizon covering this singularity. It should be noted that for regular black holes, one only has to investigate the existence of the event horizon. To address the first condition, we investigate the Kretschmann scalar. Considering the metric (2.1), the Kretschmann scalar is obtained as

$$K = R_{\alpha\beta\gamma\delta}R^{\alpha\beta\gamma\delta} = \frac{H(a, \theta, q_e, q_m, k_s, k_e, k_m, \Lambda)}{(r^2 + a^2 \cos^2 \theta)^6} \quad (2.3)$$

where H is a polynomial function. We find that the Kretschmann scalar diverges at $r = 0$ and $\theta = \pi/2$ when $r^2 + a^2 \cos^2 \theta = 0$ and goes to $\frac{8}{3}\Lambda^2$ as $r \rightarrow \infty$. So there is a singularity at $r = 0$. Now, we investigate the presence of event horizon for the solution. Here we study two separate cases, the case of positive d_1 and e_1 (Case I), and the case of negative d_1 and e_1 (Case II). As we know, the horizons are given by the zeros of g_{rr}^{-1} . To investigate the effects of

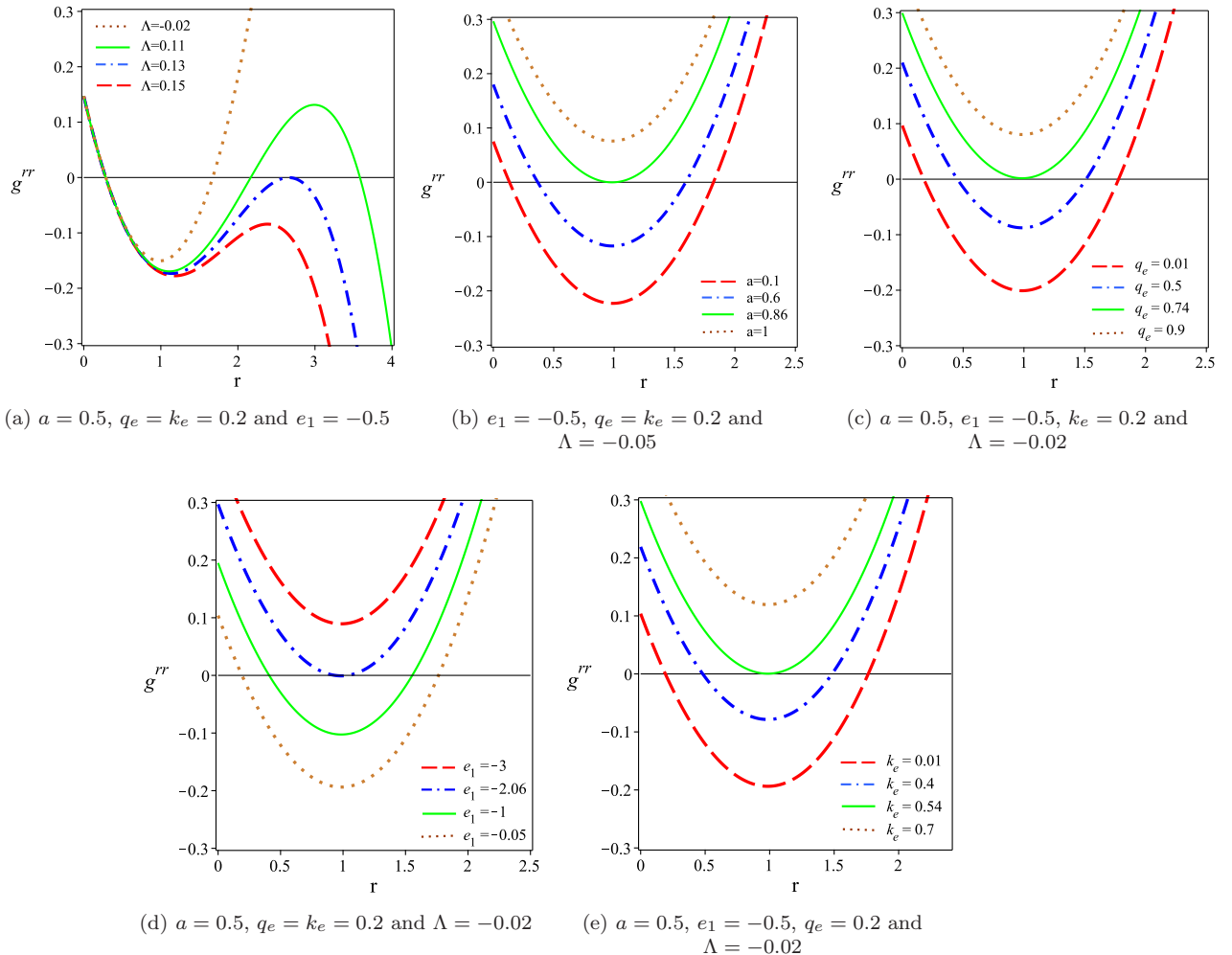


FIG. 2: The function g^{rr} versus r for $k_s = 10^{-6}$, $q_m = k_m = 0.2$, $d_1 = -0.5$ and $M = 1$.

different parameters on number of roots, we have plotted different diagrams in Figs. 1 (case I) and 2 (case II). Fig. 1 displays that the solution could admit up to two roots if suitable values are considered for different parameters. Since the event horizon is defined as outer root of g_{rr}^{-1} when its slope is positive, from Fig. 1(a), one can find that the corresponding solution is covered by an event horizon for $\Lambda < 0$. Figs. 1(b) and 1(c) display that the existence of root, hence black hole solution is bounded by an upper limit of rotation parameter and electric charge. This reveals the fact that for highly electrically charged solutions and or fast-rotating ones, the roots of g^{rr} will disappear. This results in solutions being a naked singularity. Therefore, there is a certain value of electric charge and rotation parameter that must not be crossed to remain the object as a black hole. According to Figs. 1(d) and 1(e), it is clear that for all values of the parameter e_1 and electric dilation charge k_e , there is at least a root for the function g^{rr} . For very small values of these two parameters, two roots can be observed, whereas, for intermediate or large values of this parameter, there is only one root. From Figs. 2(d) and 2(e) can be seen that in contrast to case I, in case II, the existence of the root is bounded by a lower (an upper) limit of the parameter e_1 (electric dilation charge k_e) such that for $e_1 < -2.06$ and $k_e > 0.54$ no root is observed. Comparing Fig. 1(a) to Fig. 2(a), one can find that more slowly rotating BH solutions in case I have only one root, whereas such BH solutions have two roots in case II (compare the red dashed curves of these two figures with each other).

It is worth mentioning that according to our analysis, there is a difference between charged rotating BHs in Weyl-Cartan theory and the standard Kerr-Newman (KN) BH with electromagnetic fields of GR. For the standard KN case, there are three different cases for the metric function: i) two real roots which are Cauchy and event horizons. ii) One real root (extreme horizon). iii) Absence of real root (naked singularity). While for such BHs in Weyl-Cartan theory, four different cases can be observed for the metric function. i) Absence of an inner Cauchy horizon and the

existence of a unique event horizon). ii) Cauchy and event horizons. iii) extreme horizon. iv) naked singularity. See Fig. 1(b) for better understanding. For more clarification, we explore the roots of a special case ($\Lambda = 0$). In this case, the roots are obtained as

$$r_{\pm} = M \pm \sqrt{M^2 + A} \quad (2.4)$$

where $A = a^2 + q_e^2 + q_m^2 + d_1 k_s^2 - 4e_1(k_e^2 + k_m^2)$. For $0 < A < M^2$, there are two real roots (Cauchy and event horizon). For the extreme case ($A = M^2$), both horizons coincide. For $A > M^2$, the solution does not contain any horizon (naked singularity). A special situation occurs for $A < 0$ i.e. $(4e_1(k_e^2 + k_m^2) > a^2 + q_e^2 + q_m^2 + d_1 k_s^2)$ such that the Cauchy horizon disappears and remains only an event horizon.

III. OPTICAL FEATURES OF THE BLACK HOLE SPACETIME

In this section, we present an in-depth study of the optical features of the black hole in WCT, given by the solution (2.2), such as the shadow geometrical shape and the energy emission rate. Taking into account these optical quantities, we inspect the effects on the black hole solution by varying the parameters of the theory.

A. Particle motion and BH shadow

In WCT, in general, the particle motion is different than the geodesic one. In the theory that we are interested, it was verified in [31] that for bosonic particles (such as light), the non-geodesic motion of the particles coincides with the geodesic equation. This means that for particles with spin, the geodesic would be modified. For our study, we will just concentrate on particle motion related to light, so that, the geodesic equation holds for our theory.

When a black hole is situated between a bright object and an observer it will cast a shadow. The apparent shape of a black hole is defined by the boundary of the shadow. To study the black hole shadow, we need to investigate the motion of a particle in the BH background. To do so, we take into account the Hamilton-Jacobi method in the black hole spacetime as [33, 34]

$$\frac{\partial S}{\partial \sigma} = -\frac{1}{2} g^{\mu\nu} \frac{\partial S}{\partial x^\mu} \frac{\partial S}{\partial x^\nu}, \quad (3.1)$$

where σ is an affine parameter, $g^{\mu\nu}$ is the metric tensor and S is Jacobian action which takes the form

$$S = -\frac{1}{2} m^2 \sigma + Et - L\phi + S_r(r) + S_\theta(\theta), \quad (3.2)$$

in which m is the mass of the test particle and $S_r(r)$ and $S_\theta(\theta)$ are the function of r and θ . Here, $E = p_t$ and $L = p_\phi$ are the conserved energy and angular momentum, respectively. Using the variable separable method and inserting Eq. (3.2) into Eq. (3.1), we obtain the equations of motion for photon ($m = 0$) as

$$\Sigma \frac{dt}{d\sigma} = \frac{r^2 + a^2}{\Delta(r)} [E(r^2 + a^2) - aL] - \frac{a}{\Delta(\theta)} [aE \sin^2 \theta - L], \quad (3.3)$$

$$\Sigma \frac{dr}{d\sigma} = \sqrt{\mathcal{R}(r)}, \quad (3.4)$$

$$\Sigma \frac{d\theta}{d\sigma} = \sqrt{\Theta(\theta)}, \quad (3.5)$$

$$\Sigma \frac{d\phi}{d\sigma} = \frac{a}{\Delta(r)} [E(r^2 + a^2) - aL] - \left(\frac{aE}{\Delta(\theta)} - \frac{L}{\Delta(\theta) \sin^2 \theta} \right), \quad (3.6)$$

where $\Delta(r)$ and $\Delta(\theta)$ are defined as

$$\Delta(r) = (1 - \frac{1}{3}\Lambda r^2)(r^2 + a^2) - 2Mr + q_e^2 + q_m^2 + d_1 k_s^2 - 4e_1(k_e^2 + k_m^2), \quad (3.7)$$

$$\Delta(\theta) = 1 + \frac{1}{3}\Lambda a^2 \cos^2 \theta, \quad (3.8)$$

also the expression $\mathcal{R}(r)$ and $\Theta(\theta)$ are given by

$$\mathcal{R}(r) = [E(r^2 + a^2) - aL]^2 - \Delta(r) \left[\frac{(aE - L)^2}{\Delta(\theta)} + \mathcal{K} \right], \quad (3.9)$$

$$\Theta(\theta) = \mathcal{K}\Delta(\theta) - \left(\frac{L^2}{\sin^2 \theta} - a^2 E^2 \right) \cos^2 \theta, \quad (3.10)$$

in which \mathcal{K} is a constant of separation called Carter constant. These equations define the propagation of photon around the spacetime of the corresponding rotating black hole. For $\mathcal{K} = 0$, θ -motion is suppressed, and all photon orbits are restricted only to a plane ($\theta = \pi/2$), yielding unstable circular orbits at the equatorial plane. Obtaining the boundary of the black hole shadow demands the study of the radial equation. We can rewrite the radial geodesic equation in terms of the effective potential V_{eff} as

$$\Sigma^2 \left(\frac{dr}{d\sigma} \right)^2 + V_{\text{eff}} = 0.$$

Introducing two impact parameters ξ and η [35] as

$$\xi = L/E, \quad \eta = \mathcal{K}/E^2, \quad (3.11)$$

the effective potential V_{eff} takes the following form

$$V_{\text{eff}} = \Delta(r) \left(\eta + \frac{(a - \xi)^2}{\Delta(\theta)} \right) - (r^2 + a^2 - a \xi)^2, \quad (3.12)$$

where we have replaced V_{eff}/E^2 by V_{eff} . Due to the constraint $\frac{dr}{d\sigma} \geq 0$, we expect that the effective potential satisfies $V_{\text{eff}} \leq 0$. When incoming photons, which are coming towards the black hole from a light source, get near the black hole, they follow the three possible trajectories. Either they have negative effective potential and fall into the BH inevitably, or their effective potential is positive and they are scattered away from the black hole, or their effective potential is zero and they make a circular orbit near the black hole. The boundary of the shadow is mainly determined by the circular photon orbit, which satisfies the following conditions

$$V_{\text{eff}}(r_{ph}) = 0, \quad \frac{dV_{\text{eff}}(r_{ph})}{dr} = 0, \quad (3.13)$$

whereas instability of orbits obeys condition

$$\frac{d^2 V_{\text{eff}}(r_{ph})}{dr^2} < 0, \quad (3.14)$$

Solving Eq. (3.13), the critical impact parameters which determine the contour of the shadow for the photon orbits around the black hole are obtained as

$$\xi_c = \frac{(r_{ph}^2 + a^2)\Delta'(r_{ph}) - 4r_{ph}\Delta(r_{ph})}{a\Delta'(r_{ph})}, \quad (3.15)$$

$$\eta_c = \frac{r_{ph}^2 \left[16\Delta(r_{ph})(a^2\Delta(\theta) - \Delta(r_{ph})) + 8r_{ph}\Delta(r_{ph})\Delta'(r_{ph}) - r_{ph}^2\Delta'(r_{ph})^2 \right]}{a^2\Delta'(r_{ph})^2\Delta(\theta)}. \quad (3.16)$$

To obtain the apparent shape of the BH shadow, we introduce the celestial coordinates x and y as follows [36]

$$\begin{aligned} x &= \lim_{r_0 \rightarrow \infty} \left(-r_0^2 \sin \theta_0 \frac{d\varphi}{dr} \Big|_{(r_0, \theta_0)} \right), \\ y &= \lim_{r_0 \rightarrow \infty} \left(r_0^2 \frac{d\theta}{dr} \Big|_{(r_0, \theta_0)} \right), \end{aligned} \quad (3.17)$$

in which θ_0 is the inclination angle. We take the limit $r \rightarrow \infty$, because the distance between the observer and the black hole is very large. For the corresponding solution, celestial coordinates take the form

$$x = \frac{\Delta(\theta)^{-1}(a \sin \theta_0 - \xi \csc \theta_0)}{\sqrt{1 - \frac{\Lambda}{3} \left[\eta + \frac{(a - \xi)^2}{\Delta(\theta)} \right]}}, \quad y = \pm \sqrt{\frac{\eta \Delta(\theta) + a^2 \cos^2 \theta_0 - \xi^2 \cot^2 \theta_0}{1 - \frac{\Lambda}{3} \left[\eta + \frac{(a - \xi)^2}{\Delta(\theta)} \right]}}. \quad (3.18)$$

TABLE I: The event horizon (r_e), photon sphere radius (r_{ph}) and shadow radius (r_{sh}) for the variation of a , q_e , k_e , e_1 and Λ for $q_m = k_m = 0.2$, $d_1 = 0.5$, $k_s = 10^{-6}$, and $M = 1$.

a	0.1	0.4	0.7	1.04
r_e ($q_e = k_e = 0.2$, $e_1 = 0.5$, $\Lambda = -0.02$)	1.9831	1.9096	1.7222	$0.98 + 0.12I$
r_{ph} ($q_e = k_e = 0.2$, $e_1 = 0.5$, $\Lambda = -0.02$)	3.0483	2.9852	2.8321	2.4708
r_{sh} ($q_e = k_e = 0.2$, $e_1 = 0.5$, $\Lambda = -0.02$)	4.8347	4.8078	4.7414	4.5678
$r_{ph} > r_e$	✓	✓	✓	✗
$r_{sh} > r_{ph}$	✓	✓	✓	✓
q_e	0.1	0.4	0.7	0.93
r_e ($a = e_1 = 0.5$, $k_e = 0.2$, $\Lambda = -0.02$)	1.8781	1.7969	1.5782	$0.98 + 0.05I$
r_{ph} ($a = e_1 = 0.5$, $k_e = 0.2$, $\Lambda = -0.02$)	2.9665	2.8588	2.5838	2.1332
r_{sh} ($a = e_1 = 0.5$, $k_e = 0.2$, $\Lambda = -0.02$)	4.8113	4.7053	4.4368	4.0185
$r_{ph} > r_e$	✓	✓	✓	✗
$r_{sh} > r_{ph}$	✓	✓	✓	✓
k_e	0.2	0.8	1.4	2
r_e ($a = e_1 = 0.5$, $q_e = 0.2$, $\Lambda = -0.02$)	1.8625	2.3438	3.0241	3.7275
r_{ph} ($a = e_1 = 0.5$, $q_e = 0.2$, $\Lambda = -0.02$)	2.9456	3.6244	4.6340	5.7440
r_{sh} ($a = e_1 = 0.5$, $q_e = 0.2$, $\Lambda = -0.02$)	4.7907	5.4513	6.3657	7.2426
$r_{ph} > r_e$	✓	✓	✓	✓
$r_{sh} > r_{ph}$	✓	✓	✓	✓
e_1	0.01	0.5	1	1.5
r_e ($a = 0.5$, $q_e = k_e = 0.2$, $\Lambda = -0.02$)	1.7756	1.8625	1.9427	2.0163
r_{ph} ($a = 0.5$, $q_e = k_e = 0.2$, $\Lambda = -0.02$)	2.8311	2.9456	3.0537	3.1546
r_{sh} ($a = 0.5$, $q_e = k_e = 0.2$, $\Lambda = -0.02$)	4.6742	4.7868	4.8930	4.9920
$r_{ph} > r_e$	✓	✓	✓	✓
$r_{sh} > r_{ph}$	✓	✓	✓	✓
Λ	0.01	-0.05	-0.1	-0.22
r_e ($a = e_1 = 0.5$, $q_e = k_e = 0.2$)	16.2154	1.8007	1.7177	1.5666
r_{ph} ($a = e_1 = 0.5$, $q_e = k_e = 0.2$)	2.9378	2.9534	2.9666	3.0013
r_{sh} ($a = e_1 = 0.5$, $q_e = k_e = 0.2$)	5.4347	4.3317	3.7930	2.9920
$r_{ph} > r_e$	✗	✓	✓	✓
$r_{sh} > r_{ph}$	✓	✓	✓	✗

Here, we employ the definition adopted in Ref. [37]. From Eq. (3.18), it is clear that the shape of the shadow is dependent on the inclination angle θ_0 . For north pole $\theta_0 = 0$ (or equivalent south pole $\theta_0 = \pi$), the boundary of the shadow is a perfect circle. The photons that form the shadow boundary satisfy

$$\xi(r_{ph}^0) = 0, \quad (3.19)$$

and the shadow radius is

$$R_{sh} = \sqrt{\frac{a^2 + \Delta_0 \eta(r_{ph}^0)}{1 - \frac{\Lambda}{3} \left[\eta + \frac{a^2}{\Delta_0} \right]}}, \quad (3.20)$$

where $\Delta_0 = 1 + \frac{1}{3}\Lambda a^2$. For $\theta_0 \neq 0$ or π , the shape of shadow is no longer round, but distorted. The maximum distortion occurs for $\theta_0 = \pi/2$ in the equatorial plane. In such a situation, the horizontal x-direction is squeezed,

TABLE II: The event horizon (r_e), photon sphere radius (r_{ph}) and shadow radius (r_{sh}) for the variation of a , q_e , k_e , e_1 and Λ for $q_m = k_m = 0.2$, $d_1 = -0.5$, $k_s = 10^{-6}$, and $M = 1$.

a	0.1	0.3	0.5	0.87
r_e ($q_e = k_e = 0.2$, $e_1 = -0.5$, $\Lambda = -0.02$)	1.8223	1.7757	1.6731	$0.98 + 0.08I$
r_{ph} ($q_e = k_e = 0.2$, $e_1 = -0.5$, $\Lambda = -0.02$)	2.8255	2.7854	2.6999	2.3501
r_{sh} ($q_e = k_e = 0.2$, $e_1 = -0.5$, $\Lambda = -0.02$)	4.6088	4.5877	4.5459	4.3740
$r_{ph} > r_e$	✓	✓	✓	✗
$r_{sh} > r_{ph}$	✓	✓	✓	✓
q_e	0.1	0.3	0.5	0.74
r_e ($a = 0.5$, $e_1 = -0.5$, $k_e = 0.2$, $\Lambda = -0.02$)	1.6931	1.6383	1.5112	$0.98 + 0.07I$
r_{ph} ($a = 0.5$, $e_1 = -0.5$, $k_e = 0.2$, $\Lambda = -0.02$)	2.7251	2.6567	2.5055	2.1287
r_{sh} ($a = 0.5$, $e_1 = -0.5$, $k_e = 0.2$, $\Lambda = -0.02$)	4.5705	4.5038	4.3580	4.0147
$r_{ph} > r_e$	✓	✓	✓	✗
$r_{sh} > r_{ph}$	✓	✓	✓	✓
k_e	0.01	0.2	0.4	0.54
r_e ($a = 0.5$, $e_1 = -0.5$, $q_e = 0.2$, $\Lambda = -0.02$)	1.7251	1.6731	1.4837	$0.98 + 0.03I$
r_{ph} ($a = 0.5$, $e_1 = -0.5$, $q_e = 0.2$, $\Lambda = -0.02$)	2.7658	2.6999	2.4744	2.1360
r_{sh} ($a = 0.5$, $e_1 = -0.5$, $q_e = 0.2$, $\Lambda = -0.02$)	4.6103	4.5459	4.3284	4.0209
$r_{ph} > r_e$	✓	✓	✓	✗
$r_{sh} > r_{ph}$	✓	✓	✓	✓
e_1	-2.07	-1	-0.5	-0.01
r_e ($a = 0.5$, $q_e = k_e = 0.2$, $\Lambda = -0.02$)	$0.98 + 0.02I$	1.5541	1.6731	1.7719
r_{ph} ($a = 0.5$, $q_e = k_e = 0.2$, $\Lambda = -0.02$)	2.1373	2.5552	2.6999	2.8262
r_{sh} ($a = 0.5$, $q_e = k_e = 0.2$, $\Lambda = -0.02$)	4.0220	4.4056	4.5459	4.6694
$r_{ph} > r_e$	✗	✓	✓	✓
$r_{sh} > r_{ph}$	✓	✓	✓	✓
Λ	-0.05	-0.1	-0.15	-0.27
r_e ($a = 0.5$, $e_1 = -0.5$, $q_e = k_e = 0.2$)	1.61994	1.5469	1.4874	1.3779
r_{ph} ($a = 0.5$, $e_1 = -0.5$, $q_e = k_e = 0.2$)	2.7080	2.7214	2.7349	2.7679
r_{sh} ($a = 0.5$, $e_1 = -0.5$, $q_e = k_e = 0.2$)	4.1443	3.6582	3.3083	2.7533
$r_{ph} > r_e$	✓	✓	✓	✓
$r_{sh} > r_{ph}$	✓	✓	✓	✗

while the vertical y-direction is elongated, but the shadow remains convex. For $y = 0$, there are two real solutions

$$\eta(r_{ph}^\pm) = 0, \quad \text{with} \quad r_{ph}^+ \geq r_{ph}^- \quad (3.21)$$

The size of the shadow is obtained as

$$r_{sh} = \frac{1}{2} (x(r_{ph}^+) - x(r_{ph}^-)). \quad (3.22)$$

For general inclination angle, r_{ph}^\pm can be determined by requiring $y(r, \theta_0) \Big|_{r=r_{ph}^\pm} = 0$, and the shadow size is then again formally given by (3.22). It is important that the roots of the above equation r_{ph}^\pm must be chosen that both are outside of the horizon. When r_{ph}^- is smaller than the horizon, one should define $r_{ph}^- = r_e$, where r_e is radius related to the event horizon. For $r_{ph}^- = r_{ph}^+$, the shadow becomes round sphere.

To observe an acceptable optical behavior, we need to investigate the condition $r_e < r_{ph} < r_{sh}$. It helps us to find admissible regions of parameters of the model for having an acceptable physical result. Since it is not possible to solve the equations analytically, we employ numerical methods to obtain the photon sphere radius and shadow radii. Several values of the event horizon, the photon sphere radius, and shadow radius are listed in table I (case I) and table II (case II). From table I, one can find that the increase of the rotation parameter and electric charge lead to an imaginary event horizon, meaning that an acceptable optical result can be observed only for limited regions of these two parameters. Regarding the effect of these two parameters on the event horizon, photon sphere radii and shadow size, we notice that both parameters have a decreasing contribution to these quantities. A remarkable point regarding the magnetic charge effect is that according to our investigation, its effect on these three quantities is the same as that of electric charge. The study of the electric dilation charge (k_e) effect shows that the increase of this parameter leads to increasing every three quantities and also an acceptable optical behavior can be observed for all values of this parameter. From the fourth row of table I, it is evident that the effect of parameter e_1 on these three quantities is just like the k_e effect. Investigating the influence of the cosmological constant on the radius of the event horizon, photon sphere radii, and shadow size, we find that increasing this parameter makes decreasing (increasing) the event horizon and shadow radii (photon sphere radius). According to table II, unlike case I, in case II, acceptable optical behavior cannot be observed for all values of k_e and e_1 . In other words, only for limited regions of these two parameters, an acceptable optical result can be found. Also, in case II, both parameters k_e and e_1 have a decreasing contribution to the event horizon, the photon sphere radius, and shadow radius which is opposite to the behavior observed in the case I.

Figure 3 displays the effect of BH parameters on the shadow size for the case II. From Figs. 3(a) and 3(b), it can be seen that deformation in shapes of the shadow gets more significant with the increasing the inclination angle θ_0 and rotation parameter a . Regarding the influence of electric charge, electric dilation parameter, and parameter e_1 on the shape of shadow, we see that although increasing q_e , k_e and $|e_1|$ makes more distortion on the shadow size, this deformation is negligible as compared to θ_0 and a . To avoid repetition, we omit drawing the figure for the case I.

B. Energy emission rate

In this subsection, we will discuss the rate of energy emission from the rotating black hole (2.1). It was shown that for a far distant observer, the BH shadow corresponds to the high energy absorption cross-section of the BH, which oscillates around a constant limiting value σ_{lim} [38, 39]. Since the shadow measures the optical appearance of a BH, it is approximately equal to the area of the photon sphere ($\sigma_{lim} \approx \pi r_{sh}^2$). The observable r_{sh} which designates approximately the size of the shadow, can be calculated as

$$r_{sh} = \frac{(x_t - x_r)^2 + y_t^2}{2|x_t - x_r|}. \quad (3.23)$$

The energy emission rate of the black hole is thus defined by

$$\frac{d^2 E(\omega)}{dtd\omega} = \frac{2\pi^3 \omega^3 r_{sh}^2}{e^{\frac{\omega}{T}} - 1}, \quad (3.24)$$

where ω is the frequency of the photon and T represents the temperature of the black hole. Since Hawking temperature depends on the geometrical properties of the spacetime (surface gravity) such as metric tensor and its symmetrical properties, we need to obtain Killing vectors to calculate Hawking temperature. The corresponding Killing vector field is $\chi = \partial/\partial t + \Omega\partial/\partial\phi$ in which $\Omega = -g_{\phi t}/g_{\phi\phi}$ is the rotational velocity of the BH horizon determined as

$$\Omega = \frac{a}{a^2 + r_e^2}. \quad (3.25)$$

The surface gravity which is related to the Hawking temperature of BHs ($T = \kappa/2\pi$) is defined as

$$\kappa = \sqrt{-\frac{1}{2}(\partial_\mu\chi_\nu)(\partial^\mu\chi^\nu)}. \quad (3.26)$$

Hence, Hawking temperature is calculated as

$$T = \frac{-3\Lambda r_e^4 + (3 - \Lambda a^2)r_e^2 - 3d_1 k_s^2 + 12e_1(k_e^2 + k_m^2) - 3a^2 - 3(q_e^2 + q_m^2)}{12\pi r_e(a^2 + r_e^2)}. \quad (3.27)$$

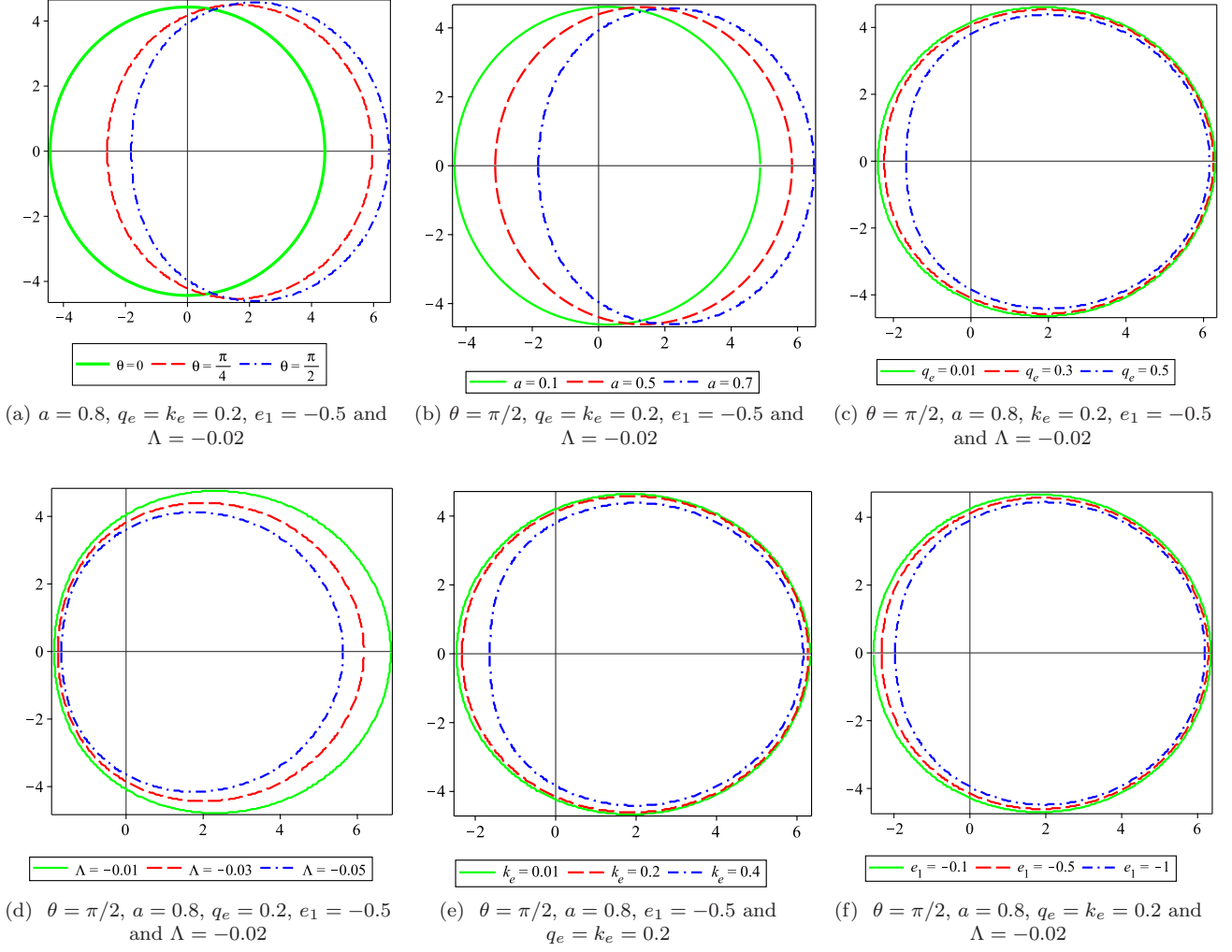


FIG. 3: Shadow cast by a charged rotating BH in WCT with $k_s = 10^{-6}$, $q_m = k_m = 0.2$, $d_1 = -0.5$, $M = 1$ and different values of θ_0 , a , q_e , k_e and Λ .

To study the radiation rate of the solution (2.1), we obtain the energy emission rate from Eq. (3.24). In Fig. 4, these energetic aspects are plotted as a function of ω for different values of the rotation parameter, electric charge, electric dilation parameter, parameter e_1 and cosmological constant for the case II. From Fig. 4(a), energy emission rate decreases as the rotation parameter increases, indicating that the evaporation process would be slow for fast-rotating BHs. To show the electric charge effect, we have plotted Fig. 4(b) which displays that this parameter decreases the energy emission so that when the BH is located in a weak electric field, the evaporation process would be faster. Studying the impact of the electric dilation parameter and parameter $|e_1|$, we observe that their effect on the emission rate is similar to that of the rotation parameter and electric charge (see Figs. 4(c) and 4(d)). Regarding the influence of the cosmological constant on the emission rate, our findings show that increasing $|\Lambda|$ leads to decreasing this optical quantity. Since the cosmological constant is proportional to AdS radius which is representing the natural curvature of the spacetime, one can find that the black hole has a longer lifetime in a high curvature background. According to our findings, unlike case II, in case I, increasing the electric dilation parameter and parameter e_1 leads to increasing the emission rate.

IV. CONSTRAINTS FROM THE EHT OBSERVATIONS

In this section, we try to consider Kerr-Newman black holes in WCT as a supermassive black hole in M87* and SgrA*, and use the EHT observations to further constrain the model parameters. Such a study can be a possible

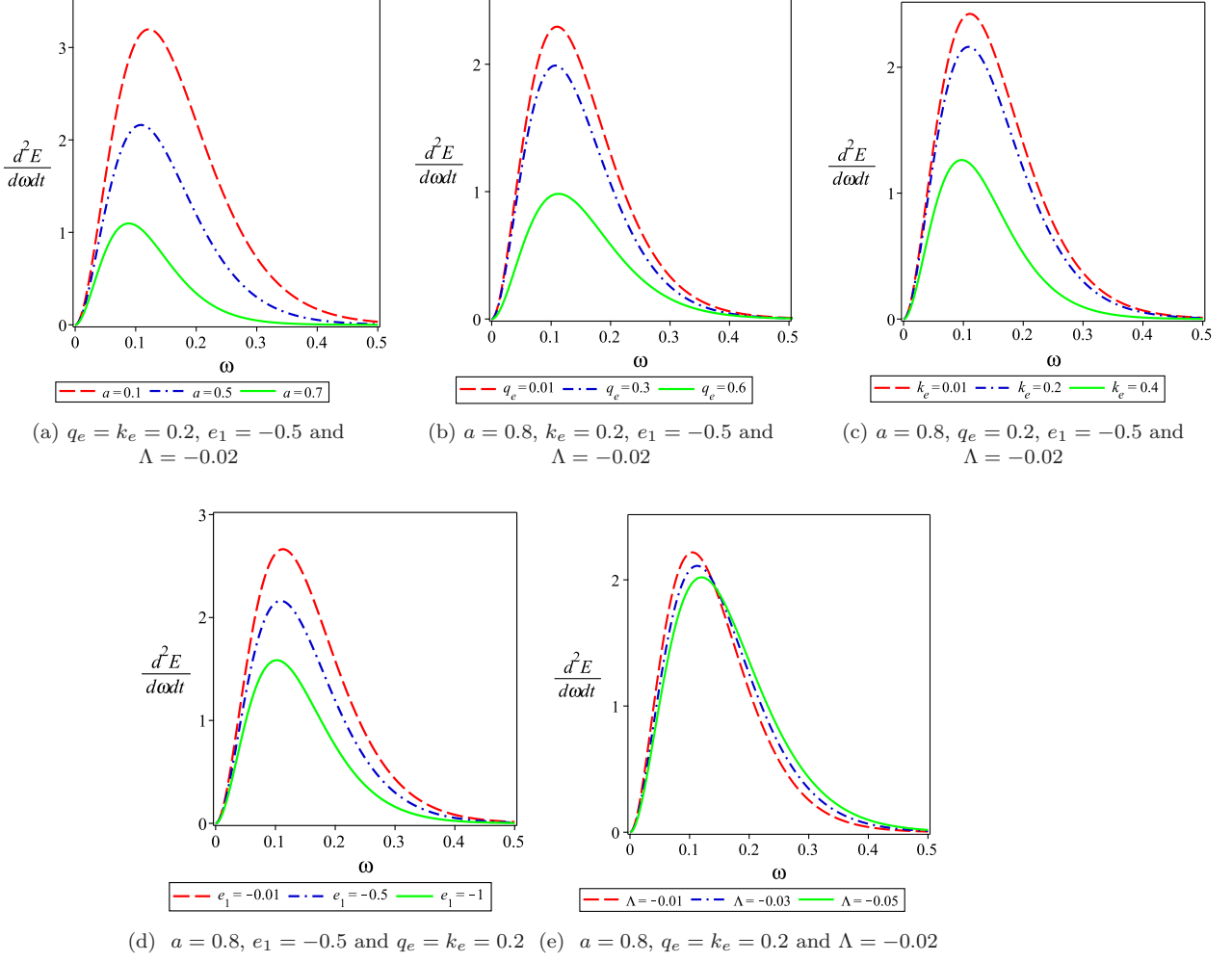


FIG. 4: The energy emission rate versus ω for the corresponding BH with $k_s = 10^{-6}$, $q_m = k_m = 0.2$, $d_1 = -0.5$, $M = 1$ and different values of a , q_e , k_e and Λ .

way to estimate the BH parameters or to distinguish modified gravity from general relativity. In this regard, we will assume that supermassive black holes might be endowed with intrinsic properties of matter.

As already mentioned, we aim to properly understand the mentioned model to explore its validity. To do so, we first define some astronomical observables which are helpful to test the parameters associated with the mentioned theory of gravity. To carefully study the influence of BH parameters on the distortion and size of the shadow, we need to connect them with shadow observables. There are different observables that can be defined via the coordinate of the shadow boundary. Hioki and Maeda proposed two observables, radius R_s and distortion δ_s to characterize the black hole shadow silhouette [40]. R_s is the radius of the reference circle for the distorted shadow which is defined as

$$R_s = \frac{(x_t - x_r)^2 + y_t^2}{2|x_r - x_t|}, \quad (4.1)$$

and δ_s is the deviation of the left edge of the shadow from the reference circle boundary given by

$$\delta_s = \frac{|x_l - x'_l|}{R_s}. \quad (4.2)$$

Notably, for the shadow of the non-rotating case, $\delta_s = 0$ due to the shape of a perfect circle. Another two characterized observables were proposed by Kumar and Ghosh in [41]. They used shadow area A and oblateness D ,

which can describe the shadow with more general shapes. Their definitions are

$$A = 2 \int y(r_p) dx(r_p) = 2 \int_{r_p^-}^{r_p^+} \left(y(r_p) \frac{dx(r_p)}{dr_p} \right) dr_p, \quad D = \frac{x_r - x_l}{y_t - y_b}. \quad (4.3)$$

Here the subscripts l , r , t and b stand for the left and right ends of the shadow silhouette, where $y(r_p) = 0$, and the top and bottom points, where $y'(r_p) = 0$, respectively. Note that for a spherically symmetric black hole shadow, it is straightforward to understand that $D = 1$, but for a Kerr shadow $\sqrt{3}/2 \leq D < 1$. The advantages of using two observables A and D are that they do not require comparing the shadow silhouette with a perfect circle and are therefore applicable to a general shadow of any shape and size.

A. Constrains on the parameters of the model from the image of M87*

In this subsection, we compare the theoretically computed shadow outline with the observed image of M87*. As reported by EHT collaboration [44], the supermassive black hole M87* at the center of the galaxy M87* has the following values

$$\theta_{M87*} = (42 \pm 3) \mu\text{as}, \quad (4.4)$$

$$M_{M87*} = (6.5 \pm 0.9) \times 10^9 M_\odot, \quad (4.5)$$

$$\mathbb{D}_{M87*} = 16.8_{-0.7}^{+0.8} \text{Mpc}, \quad (4.6)$$

where θ and \mathbb{D} are, respectively, the angular diameter of the shadow and the distance of the M87* from the Earth. M and M_\odot denote the mass of the M87* and Sun mass. These numbers imply that the diameter of the shadow in units of mass should be [43]

$$d_{M87*} \equiv \frac{\mathbb{D}\theta}{M} \approx 11.0 \pm 1.5. \quad (4.7)$$

The diameter of the shadow as a function of the rotation parameter a , electric charge q_e and cosmological constant Λ is depicted in Fig. 5 for case I. We have plotted all graphs of this figure for the inclination angle $\theta_0 = 0^\circ$ and within 1σ and 2σ uncertainties. From Fig. 5(a), data for M87* black hole gives bound on the electric charge such that the resulting shadow of slowly rotating black holes is within 1σ uncertainty for $q_e \leq 0.407$ and within 2σ uncertainty for $0.407 < q_e \leq 0.992$, whereas for $q_e > 0.992$ the shadow is not in agreement with EHT data (see solid curve in Fig. 5(a)). For intermediate values of the rotation parameter, d_{sh} is located in 1σ (2σ) confidence region for small (large) electric charges (see dash curve in Fig. 5(a)). According to this figure, fast-rotating BHs have a shadow in agreement with observational data within the 2σ -error for all values of the electric charge (see dash dot curve in Fig. 5(a)). Fig. 5(b) shows that some constraints should be imposed on the electric dilation parameter to have consistent results with EHT data of M87*. According to red solid curve of this figure, for very small values of this parameter, d_{sh} is in agreement with observational data within 1σ -error (2σ -error) for $a \leq 0.671$ ($a > 0.671$). According to our findings, the resulting shadow becomes consistent with the detection of EHT for M87* in the region $0 < k_e < 1.835$. Figure 5(c) displays the allowed regions of the cosmological constant for which the obtained shadow is consistent with M87* shadow. As we see, for rotating BHs in a high curvature background, the resulting shadow is not agreement with EHT data. For black holes located in a low curvature background, d_{sh} is consistent with observational data within 1σ -error. For intermediate values of the cosmological constant, d_{sh} is located in 2σ confidence region for all values of the rotation parameter. To determine allowed regions of the parameter e_1 , we have plotted Fig. 5(d), showing that for very small values of e_1 , the resulting shadow of slowly (fast) rotating BHs is located in 1σ (2σ) confidence (see the solid curve of Fig. 5(d)), whereas for intermediate and large values of this parameter, d_{sh} is in agreement with observational data within 1σ -error (see dash and dash-dotted curves of Fig. 5(d)).

Fig. 6 displays the variation of d_{sh} under change of BH parameters with the inclination angle $\theta_0 = 0^\circ$ for case II. According to Fig. 6(a), fast-rotating BHs located in a weak electric field have a compatible shadow within 2σ uncertainty, whereas these BHs with powerful electric charge have no compatible shadow with EHT data (see dash-dot curve in Fig. 6(a)). For small and intermediate values of the rotation parameter, d_{sh} is located in 2σ confidence region for all values of the electric charge (see dash and solid curves in Fig. 6(a)). From Fig. 6(b), one can find the allowed region of the electric dilation parameter to have consistent results with EHT data. According to dash-dot curve of this figure, for intermediate values of this parameter, d_{sh} is in agreement with observational data within 2σ -error for $a \leq 0.685$, otherwise it is not in agreement with EHT data. This figure also shows that for rotating black holes with very small values of k_e , the resulting shadow becomes consistent with the detection of EHT within 2σ -error all

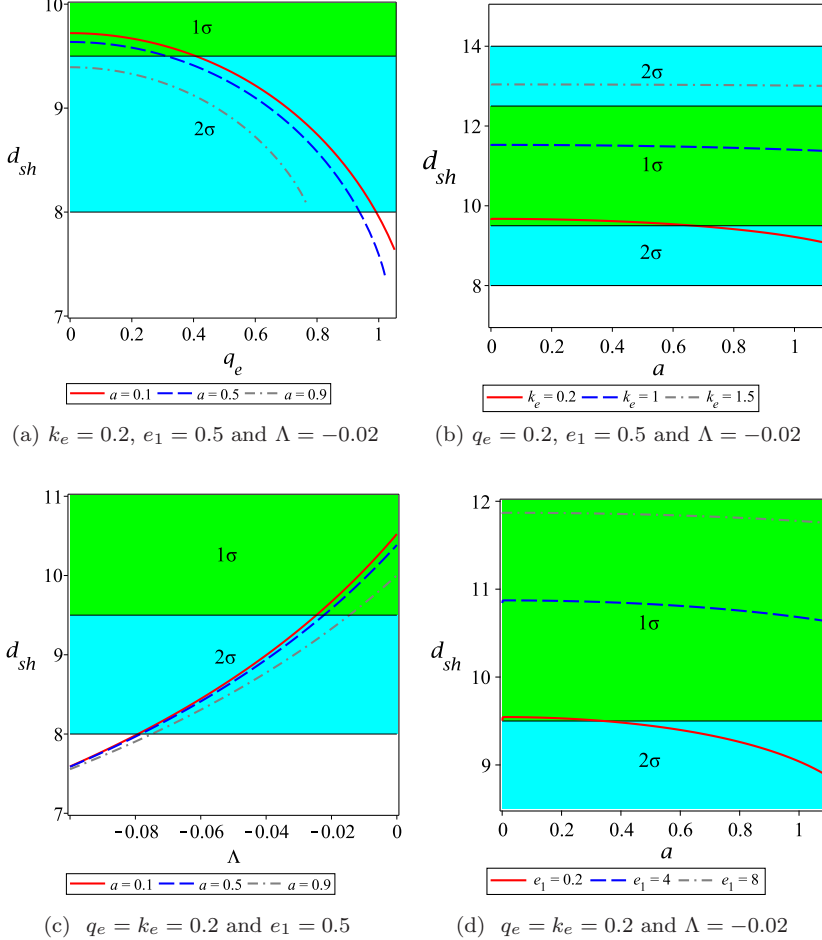


FIG. 5: The predicted diameter for a charged rotating BH in WCT for case I with $k_s = 10^{-6}$, $q_m = k_m = 0.2$, $d_1 = 0.5$ and $M = 1$ with the EHT observations of M87*. **Left-up graph:** d_{sh} as a function of q_e for fixed k_e , e_1 , Λ , and for several values of the rotation parameter. **Right-up graph:** d_{sh} as a function of the rotation parameter, for fixed q_e , e_1 , Λ , and different values of k_e . **Left-down graph:** d_{sh} as a function of the cosmological constant, for fixed q_e , k_e , e_1 , and different values of the rotation parameter. **Right-down graph:** d_{sh} as a function of the rotation parameter, for fixed q_e , k_e , Λ , and different values of e_1 . The green shaded region gives the 1σ confidence region for d_{sh} , whereas the cyan shaded region gives the 2σ confidence region. The inclination angle is $\theta_0 = 0^\circ$.

the time (see solid and dash curves of Fig. 6(b)). To find the allowed regions of the cosmological constant, we have plotted Figure 6(c). According to our analysis, a compatible result occurs in the region $-0.061 < \Lambda < 0$ which shows that the allowed region of the cosmological constant is less than that of the case I. Fig. 6(d) illustrates the allowed regions of e_1 for which the obtained shadow is consistent with M87* shadow. As is seen, for small and intermediate values of $|e_1|$ the resulting shadow is in agreement with M87* data in 2σ -error confidence region, whereas for large values of this parameter, a compatible d_{sh} is observed for $a \leq 0.582$. To have a better understanding of the effects of Weyl-Cartan geometry, we set $q_e = q_m = \Lambda = 0$ and determine the allowed regions of WC parameters to have consistent results. Comparing Fig. 7(a) to Fig. 5(d), one can find that the allowed region of e_1 parameter decreases in the absence of the electric and magnetic charges and cosmological constant for case I. While for case II, the allowed region of e_1 increases (compare Fig. 7(c) to Fig. 6(d)). From Figs. 7(b) and 5(b), it is clear that the allowed region of k_e parameter decreases for case I in the absence of q_e , q_m and Λ as well. While the opposite behavior is observed for case II (compare Fig. 7(d) to Fig. 6(b)).

Now we study two other observables which are useful to determine the allowed regions of parameters. According to results obtained in [44–46], the image of supermassive BH M87* photographed by the EHT is crescent shaped, and the EHT observations constrain the deviation from circularity as $\Delta C \lesssim 0.1$ and the axis ratio as $1 < D_x \lesssim 4/3$. To

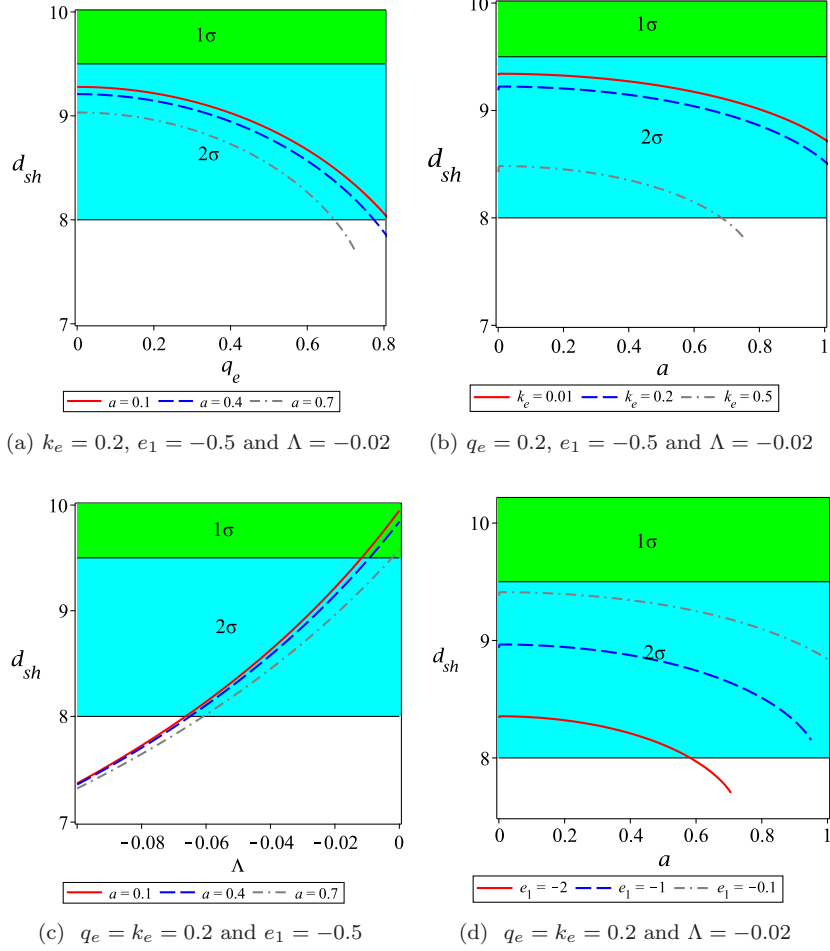


FIG. 6: The predicted diameter for a charged rotating BH in WCT for case II with $k_s = 10^{-6}$, $q_m = k_m = 0.2$, $d_1 = -0.5$ and $M = 1$ with the EHT observations of M87*. **Left-up graph:** d_{sh} as a function of q_e for fixed k_e , e_1 , and Λ , and for several values of the rotation parameter. **Right-up graph:** d_{sh} as a function of the rotation parameter, for fixed q_e , e_1 , Λ , and different values of k_e . **Left-down graph:** d_{sh} as a function of the cosmological constant, for fixed q_e , k_e , e_1 , and different values of the rotation parameter. **Right-down graph:** d_{sh} as a function of the rotation parameter, for fixed q_e , k_e , Λ , and different values of e_1 . The green shaded region gives the 1σ confidence region for d_{sh} , whereas the cyan shaded region gives the 2σ confidence region. The inclination angle is $\theta_0 = 0^\circ$.

define the circularity deviation ΔC , one has to describe the boundary of a black hole shadow in the polar coordinates

$$\phi = \tan^{-1} \left(\frac{y - y_c}{x - x_c} \right), \quad \mathbb{R}(\phi) = \sqrt{(x - x_c)^2 + (y - y_c)^2}, \quad (4.8)$$

in which the geometric center of the black hole shadow is determined by the edges of the shaped boundary via $(x_c = \frac{x_r + x_l}{2}, y_c = 0)$. The average radius of the shadow can be calculated as

$$\bar{\mathbb{R}}^2 = \frac{1}{2\pi} \int_0^{2\pi} \mathbb{R}(\phi)^2 d\phi. \quad (4.9)$$

the deviation of the shadow from circularity can be defined as

$$\Delta C = \frac{1}{\bar{\mathbb{R}}} \sqrt{\frac{1}{2\pi} \int_0^{2\pi} (\mathbb{R}(\phi) - \bar{\mathbb{R}})^2 d\phi}, \quad (4.10)$$

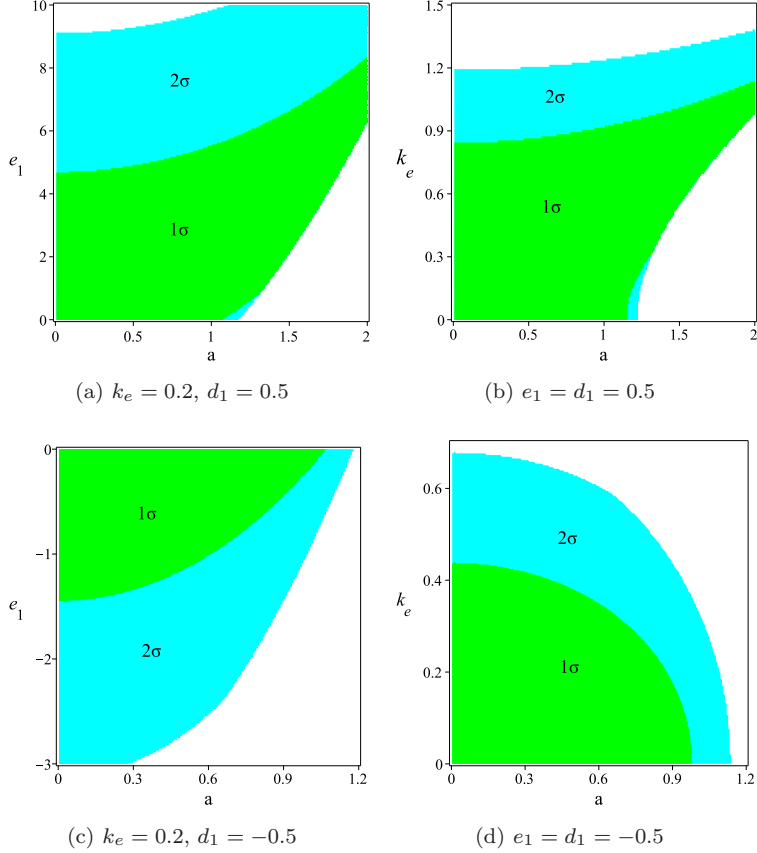


FIG. 7: constraints on the Weyl-Cartan parameters and rotation parameter for $k_s = 10^{-6}$, $k_m = 0.2$, $M = 1$ and $\theta_0 = 0^\circ$ with the EHT observations of M87*.

and the axis ratio is given as [47, 48]

$$D_x = D^{-1} = \frac{y_t - y_b}{x_r - x_l}. \quad (4.11)$$

To compare with the EHT constraints on ΔC and D_x in M87*, we have listed several values of these two quantities in Table III for both cases I and II. To better refer to the EHT observations of M87*, we have considered $\theta_0 = 17^\circ$ since the jet inclination with respect to the line-of-sight for M87* is estimated to be 17° [49]. As can be seen from this table, the EHT observations $\Delta C \lesssim 0.1$ is satisfied for the whole parameters of both cases. According to our findings, the condition $1 < D_x \lesssim 4/3$ imposes a constraint on k_e for case I such that this condition is satisfied for only $0 \leq k_e \leq 0.6$. This condition also imposes a constraint on the cosmological constant for both cases. From the fifth row of this table, one can find that the condition $1 < D_x \lesssim 4/3$ is satisfied in the range $-0.03 \leq \Lambda \leq 0$ ($-0.04 \leq \Lambda \leq 0$) for case I (II).

The recent EHT papers on M87* observation have estimated the Schwarzschild shadow deviation (δ) which measures the difference between the model shadow diameter (d_{metric}) and the Schwarzschild shadow diameter and is given by [50]

$$\delta = \frac{d_{metric}}{6\sqrt{3}} - 1, \quad (4.12)$$

where $d_{metric} = 2R_a$ with $R_a = \sqrt{A/\pi}$ and A is obtained by Eq.(4.3). Evidently, δ can be positive (negative) if the black hole shadow size is greater (smaller) than the Schwarzschild black hole of the same mass. According to results reported by the EHT observations, the bound of the measured Schwarzschild deviation is as $\delta = -0.01 \pm 0.17$ [45, 51]. Several values of δ are reported in table III which illustrates that for the whole parameters of both cases, the resulting shadow is smaller than the Schwarzschild black hole shadow. For case I, all values of the rotation parameter, electric

dilation parameter, and parameter e_1 satisfy the 1σ bound. Regarding the electric charge and cosmological constant, only the range $0 < q_e < 0.6$ and $-0.025 \leq \Lambda \leq 0$ can satisfy the 1σ bound, otherwise they satisfy the 2σ bound. For case II, the 1σ and 2σ bounds can be satisfied in the following ranges

1σ		2σ	
$0 \leq a < 0.5$		$0.5 \leq a \leq 0.8$	
$0 \leq q_e < 0.2$		$0.2 \leq q_e \leq 0.7$	
$0 \leq k_e < 0.2$		$0.2 \leq k_e \leq 0.5$	
$-0.5 < e_1 < 0$		$-2 \leq e_1 \leq -0.5$	
$-0.02 < \Lambda < 0$		$-0.04 \leq \Lambda \leq -0.02$	

TABLE III: The circularity deviation ΔC , axial ratio D_x , distortion δ_s and fractional deviation parameter δ for the variation of a , q_e , k_e , e_1 and Λ for $q_m = k_m = 0.2$, $k_s = 10^{-6}$, $M = 1$ and $\theta_0 = 17^\circ$.

Case I					Case II				
$q_e = k_e = 0.2$, $e_1 = 0.5$ and $\Lambda = -0.02$					$q_e = k_e = 0.2$, $e_1 = -0.5$ and $\Lambda = -0.02$				
a	ΔC	D_x	δ_s	δ	a	ΔC	D_x	δ_s	δ
0.2	3.34×10^{-5}	1.00009	1.89×10^{-4}	-0.13547	0.1	1.61×10^{-5}	1.00005	9.04×10^{-5}	-0.16987
0.4	1.58×10^{-4}	1.00045	8.93×10^{-4}	-0.13920	0.3	1.63×10^{-4}	1.00045	9.05×10^{-4}	-0.17310
0.6	4.71×10^{-4}	1.0013	2.64×10^{-3}	-0.14592	0.5	5.58×10^{-4}	1.0015	3.14×10^{-3}	-0.18006
0.8	1.25×10^{-3}	1.0035	6.97×10^{-3}	-0.15666	0.7	1.60×10^{-3}	1.0045	8.99×10^{-3}	-0.19215
1.0	3.69×10^{-3}	1.0102	2.02×10^{-2}	-0.17423	0.8	2.83×10^{-3}	1.0079	1.57×10^{-2}	-0.20122
$a = 0.5$, $k_e = 0.2$, $e_1 = 0.5$ and $\Lambda = -0.02$					$a = 0.5$, $k_e = 0.2$, $e_1 = -0.5$ and $\Lambda = -0.02$				
q_e	ΔC	D_x	δ_s	δ	q_e	ΔC	D_x	δ_s	δ
0.1	2.62×10^{-4}	1.0007	1.47×10^{-3}	-0.13895	0.1	5.22×10^{-4}	1.0014	2.94×10^{-3}	-0.17615
0.3	3.13×10^{-4}	1.0008	1.76×10^{-3}	-0.14759	0.3	6.24×10^{-4}	1.0017	3.51×10^{-3}	-0.18677
0.5	4.40×10^{-4}	1.0012	2.47×10^{-3}	-0.16613	0.5	9.17×10^{-4}	1.0025	5.15×10^{-3}	-0.21020
0.7	7.51×10^{-4}	1.0021	4.22×10^{-3}	-0.19807	0.6	1.25×10^{-3}	1.0035	7.02×10^{-3}	-0.22856
0.9	1.99×10^{-3}	1.0056	1.11×10^{-2}	-0.25385	0.7	1.99×10^{-3}	1.0056	1.11×10^{-2}	-0.25385
$a = 0.5$, $q_e = 0.2$, $e_1 = 0.5$ and $\Lambda = -0.02$					$a = 0.5$, $q_e = 0.2$, $e_1 = -0.5$ and $\Lambda = -0.02$				
k_e	ΔC	D_x	δ_s	δ	k_e	ΔC	D_x	δ_s	δ
0.01	3.33×10^{-4}	1.00094	1.87×10^{-3}	-0.15091	0.1	4.89×10^{-4}	1.0013	2.75×10^{-3}	-0.17233
0.2	2.80×10^{-4}	1.00079	1.57×10^{-3}	-0.14214	0.2	5.58×10^{-4}	1.0015	3.14×10^{-3}	-0.18006
0.4	1.54×10^{-4}	1.00045	8.93×10^{-4}	-0.11793	0.3	7.10×10^{-4}	1.0019	3.93×10^{-3}	-0.19374
0.6	3.15×10^{-5}	1.00008	1.59×10^{-4}	-0.08305	0.4	9.93×10^{-4}	1.0028	5.58×10^{-3}	-0.21499
0.7	3.16×10^{-5}	0.99996	-1.67×10^{-4}	-0.06313	0.5	1.76×10^{-3}	1.0049	9.89×10^{-3}	-0.24757
$a = 0.5$, $q_e = k_e = 0.2$ and $\Lambda = -0.02$					$a = 0.5$, $q_e = k_e = 0.2$ and $\Lambda = -0.02$				
e_1	ΔC	D_x	δ_s	δ	e_1	ΔC	D_x	δ_s	δ
0.01	3.93×10^{-4}	1.00111	2.21×10^{-3}	-0.15976	-0.01	3.98×10^{-4}	1.0011	2.24×10^{-3}	-0.16052
0.4	3.01×10^{-4}	1.00085	1.69×10^{-3}	-0.14561	-0.4	5.20×10^{-4}	1.0014	2.93×10^{-3}	-0.17590
0.8	2.26×10^{-4}	1.00064	1.27×10^{-3}	-0.13210	-0.8	6.93×10^{-4}	1.0019	3.90×10^{-3}	-0.19317
1.2	1.66×10^{-5}	1.00074	9.32×10^{-4}	-0.11945	-1.2	9.51×10^{-4}	1.0026	5.35×10^{-3}	-0.21242
1.6	1.16×10^{-4}	1.00032	6.49×10^{-4}	-0.10755	-1.6	1.38×10^{-3}	1.0038	7.76×10^{-3}	-0.23436
$a = 0.5$, $q_e = k_e = 0.2$ and $e_1 = 0.5$					$a = 0.5$, $q_e = k_e = 0.2$ and $e_1 = -0.5$				
Λ	ΔC	D_x	δ_s	δ	Λ	ΔC	D_x	δ_s	δ
-0.01	4.20×10^{-4}	1.00119	2.37×10^{-3}	-0.07930	-0.01	6.78×10^{-4}	1.00191	3.82×10^{-3}	-0.12572
-0.02	2.80×10^{-4}	1.00079	1.57×10^{-3}	-0.14214	-0.02	5.58×10^{-4}	1.00157	3.14×10^{-3}	-0.180062
-0.03	9.18×10^{-5}	1.00024	4.88×10^{-4}	-0.19361	-0.03	3.82×10^{-4}	1.00107	2.13×10^{-3}	-0.22533
-0.04	1.40×10^{-5}	0.99961	-7.74×10^{-4}	-0.23676	-0.04	1.75×10^{-4}	1.00047	9.37×10^{-4}	-0.26381
-0.05	3.79×10^{-4}	0.99893	-2.13×10^{-3}	-0.27364	-0.05	8.98×10^{-5}	0.99980	-3.82×10^{-4}	-0.29706

B. Constrains on the parameters of the model from the image of Sgr A*

In this subsection, we are going to model Sgr A* as the rotating BHs in WCT and impose the EHT-inferred bounds on d_{sh} , D , and δ to find the constraints on the parameters. The results obtained from EHT observations showed that the Sgr A* BH shadow images have advantages for testing the nature of astrophysical black holes, as the mass of the Sgr A* black hole bridges the gap between the stellar black holes observed by the LIGO and the M87* black hole. Therefore, it can probe a significant curvature scale (10⁶ orders of curvature higher than M87*). According to the EHT collaboration, the image of Sgr A* is consistent with an expected appearance of the Kerr black hole with an inferred BH mass $M = (4.3 \pm 0.013) \times 10^6 M_\odot$ and distance $D = 8277 \pm 33 pc$ from earth [50]. In contrast to the M87* black hole, for which the EHT only measured the emission ring diameter, for Sgr A*, the EHT not only estimated the emission ring angular diameter $\theta_d = (51.8 \pm 2.3) \mu as$ but also could provide an estimate of the shadow diameter $\theta_{sh} = (48.7 \pm 7) \mu as$ [52]. Using these reported expressions, the diameter of the shadow image for Sgr. A* is obtained as

$$d_{Sgr.A*} \equiv \frac{D\theta_{sh}}{M} \approx 9.5 \pm 1.4. \quad (4.13)$$

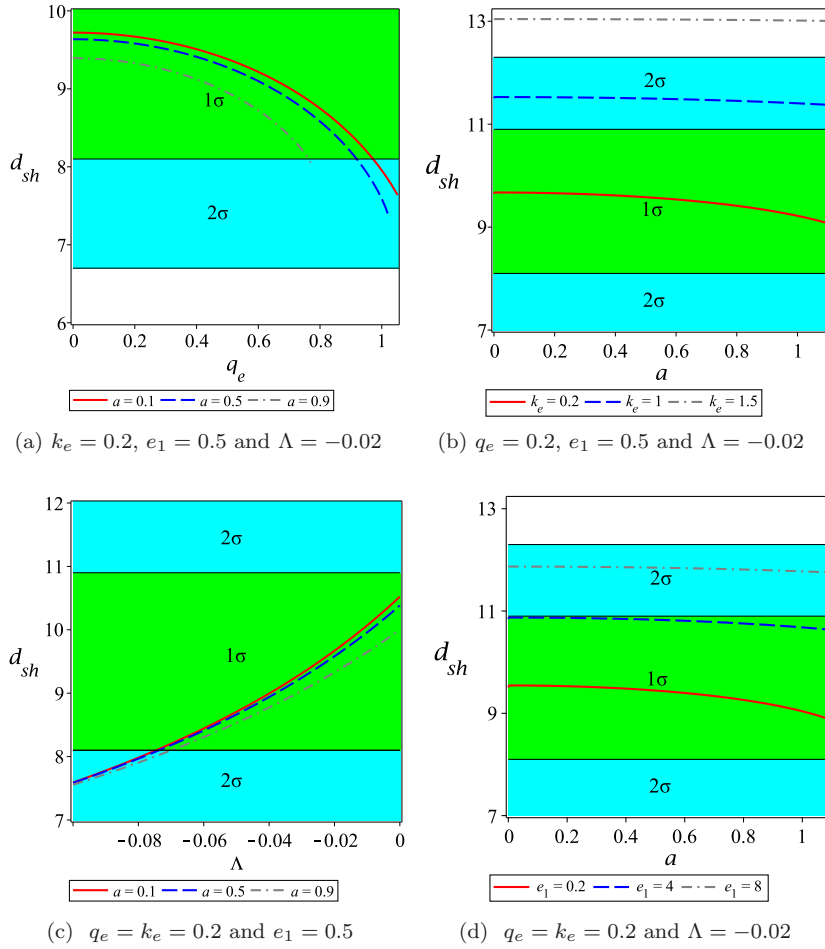


FIG. 8: The predicted diameter for a charged rotating BH in WCT for case I with $k_s = 10^{-6}$, $q_m = k_m = 0.2$, $d_1 = 0.5$ and $M = 1$ with the EHT observations of Sgr A*. **Left-up graph:** d_{sh} as a function of q_e for fixed k_e , e_1 , and Λ , and for several values of the rotation parameter. **Right-up graph:** d_{sh} as a function of the rotation parameter, for fixed q_e , e_1 , Λ , and different values of k_e . **Left-down graph:** d_{sh} as a function of the cosmological constant, for fixed q_e , k_e , e_1 , and different values of the rotation parameter. **Right-down graph:** d_{sh} as a function of the rotation parameter, for fixed q_e , k_e , Λ , and different values of e_1 . The green shaded region gives the 1σ confidence region for d_{sh} , whereas the cyan shaded region gives the 2σ confidence region. The inclination angle is $\theta_0 = 0^\circ$.

To explore the effect of BH parameters on d_{sh} , Figs. 8 (case I) and 9 (case II) have been drawn for the inclination angle $\theta_0 = 0^\circ$. Taking a look at Fig. 8, one can find that the resulting shadow of fast-rotating black holes is within 1σ uncertainty according to data for Sgr A* (see dash dot curve in Fig. 8(a)). For slowly rotating black holes, d_{sh} becomes consistent with EHT data within 1σ -error for $q_e \leq 0.972$, otherwise it is in agreement with observations within 2σ uncertainty (see solid curve in Fig. 8(a)). It is clear from this figure that the resulting shadow of Kerr-Newman black holes in WCT for case I is consistent with Sgr A* shadow for all values of the electric charge. To find some constraints on the electric dilation parameter to have consistent results with EHT data of Sgr A*, we have plotted Fig. 8(b) which shows that rotating black holes with very small values of k_e have a compatible result with EHT data within 1σ uncertainty. According to our analysis, no compatible result can be observed with Sgr A* data for $k_e > 1.27$. Figure 8(c) displays the allowed regions of the cosmological constant for which the obtained shadow is consistent with Sgr A* shadow. As we see, for rotating BHs in a high curvature background, d_{sh} becomes consistent with EHT data within 2σ uncertainty, otherwise it is in agreement with observations in 1σ -error confidence region. From Fig 8(d), one finds allowed regions of the parameter e_1 , showing that for small and intermediate values of e_1 , the resulting shadow is in agreement with observational data within 1σ -error, whereas for large values d_{sh} is located within 2σ -error.

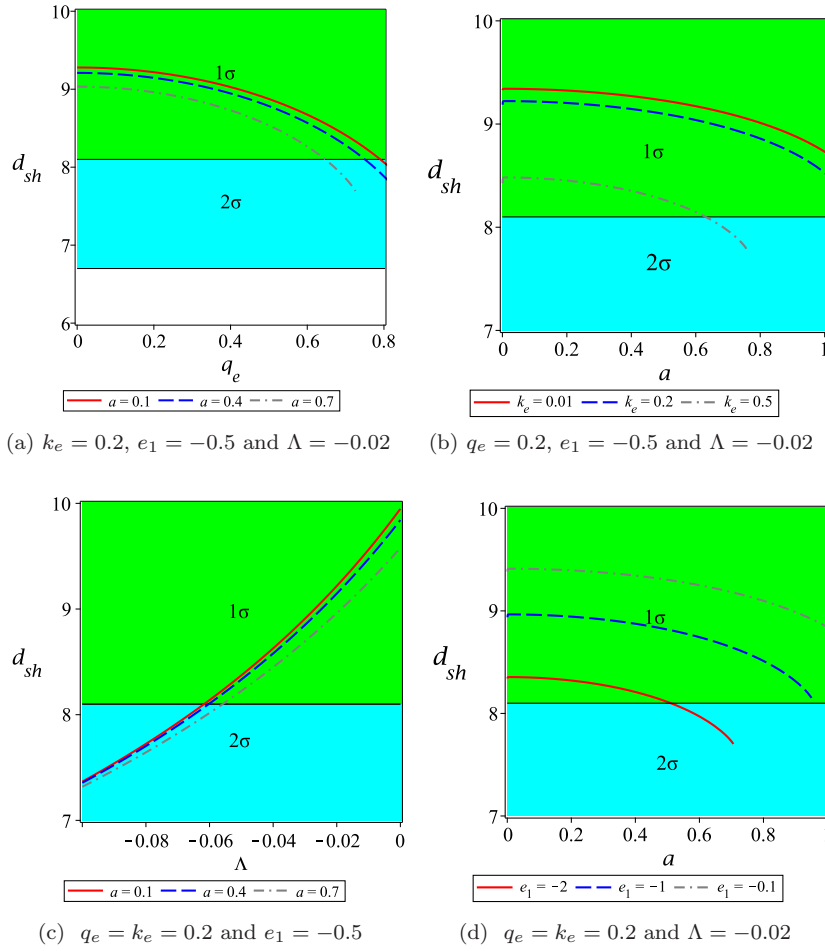


FIG. 9: The predicted diameter for a charged rotating BH in WCT for case II with $k_s = 10^{-6}$, $q_m = k_m = 0.2$, $d_1 = -0.5$ and $M = 1$ with the EHT observations of Sgr A*. **Left-up graph:** d_{sh} as a function of q_e for fixed k_e , e_1 , and Λ , and for several values of the rotation parameter. **Right-up graph:** d_{sh} as a function of the rotation parameter, for fixed q_e , e_1 , Λ , and different values of k_e . **Left-down graph:** d_{sh} as a function of the cosmological constant, for fixed q_e , k_e , e_1 , and different values of the rotation parameter. **Right-down graph:** d_{sh} as a function of the rotation parameter, for fixed q_e , k_e , Λ , and different values of e_1 . The green shaded region gives the 1σ confidence region for d_{sh} , whereas the cyan shaded region gives the 2σ confidence region. The inclination angle is $\theta_0 = 0^\circ$.

To find the allowed regions of parameters for case II, we have plotted Fig. 9. From Fig. 9(a), data for Sgr A*

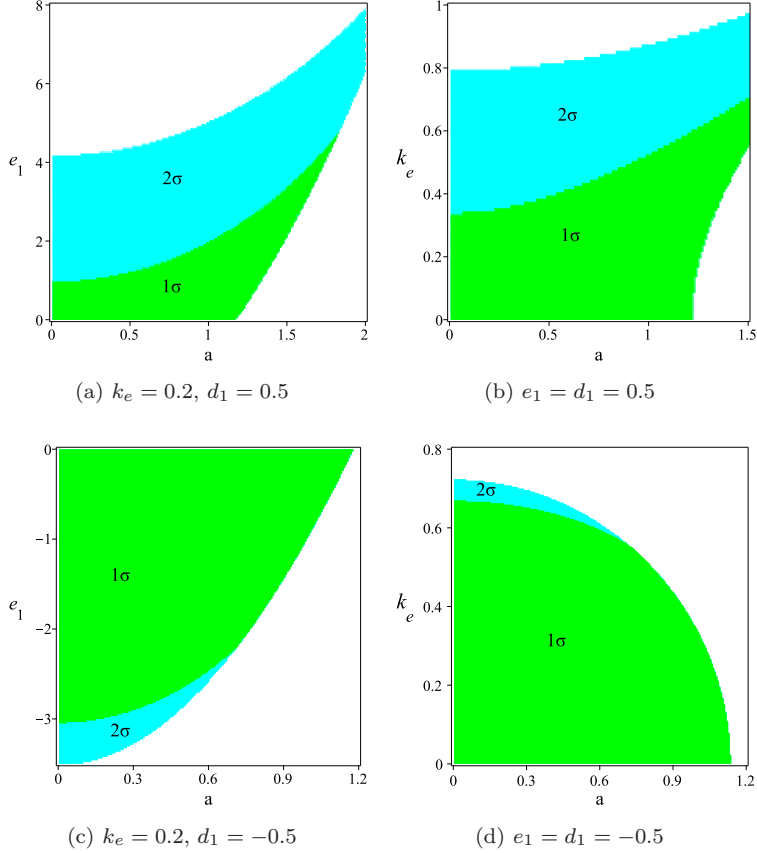


FIG. 10: constraints on the Weyl-Cartan parameters and rotation parameter for $k_s = 10^{-6}$, $k_m = 0.2$, $M = 1$ and $\theta_0 = 0^\circ$ with the EHT observations of Sgr A*.

black hole gives bound on the electric charge such that the resulting shadow of fast-rotating black holes is within 1σ uncertainty for $q_e \leq 0.63$, otherwise it is within 2σ uncertainty (see dash dot curve in Fig. 9(a)). For slowly rotating black holes, d_{sh} becomes consistent with EHT data within 1σ -error for all electric charges (see solid curve in Fig. 9(a)). Fig. 9(b) shows the influence of the electric dilation parameter on d_{sh} . According to dash-dot curve of this figure, rotating black holes with intermediate values of k_e have a compatible result with EHT data within 1σ (2σ) uncertainty for $a \leq 0.631$ ($a > 0.631$), whereas for very small values of this parameter, d_{sh} is located in 1σ confidence region according to Sgr A* data. From Fig. 9(c), we find the compatible range of the cosmological constant with EHT data. According to our analysis, for the range of $-0.056 \leq \Lambda < 0$, the diameter of shadow is located in 1σ confidence region, otherwise it is located within 2σ uncertainty. To determine allowed regions of the parameter e_1 , we have plotted Fig. 9(d). According to this figure, fast-rotating BHs with large values of $|e_1|$ have a consistent shadow with data of Sgr A* within 2σ uncertainty, whereas for small and intermediate values of $|e_1|$, d_{sh} is located within 1σ -error. In Fig. 10, we set $q_e = q_m = \Lambda = 0$ and constrain Weyl-Cartan parameters to have consistent results. Comparing this figure to figures 8 and 9, we notice that the allowed regions of WC parameters decrease (increase) for case I (case II) in the absence of the electric and magnetic charges and the cosmological constant.

Now, we calculate Schwarzschild shadow deviation δ based on observations of Sgr A*. EHT used the two separate priors for the Sgr A* shadow size from the Keck and Very Large Telescope Interferometer (VLTI) observations to estimate the bounds on the fraction deviation observable δ as follows [53]

$$\delta = \begin{cases} -0.08^{+0.09}_{-0.09} & (\text{VLTI}) \\ -0.04^{+0.09}_{-0.10} & (\text{Keck}) \end{cases} . \quad (4.14)$$

It is worthwhile to mention that the Event Horizon Telescope collaboration does not impose any constraints on ΔC and D_x for the image of Sgr A*.

Table IV lists several values of D , δ_s and δ under variation of BH parameters for both cases I and II. Here we have considered the case with $\theta_0 = 50^\circ$ because as addressed in [54] the inclination angle (with respect to the line of sight)

TABLE IV: shadow observables D , δ_s , δ for the variation of a , q_e , k_e , e_1 and Λ for $q_m = k_m = 0.2$, $k_s = 10^{-6}$, $M = 1$ and $\theta_0 = 50^\circ$.

Case I				Case II			
$q_e = k_e = 0.2$, $e_1 = 0.5$ and $\Lambda = -0.02$				$q_e = k_e = 0.2$, $e_1 = -0.5$ and $\Lambda = -0.02$			
a	D	δ_s	δ	a	D	δ_s	δ
0.2	0.99779	0.00441	-0.13618	0.1	0.99939	0.00141	-0.17005
0.4	0.99083	0.01839	-0.14208	0.3	0.99345	0.01311	-0.17477
0.6	0.97780	0.04473	-0.15256	0.5	0.97905	0.03981	-0.19168
0.8	0.95490	0.09128	-0.16918	0.7	0.95393	0.09317	-0.20259
1.0	0.90239	0.19799	-0.19840	0.8	0.92846	0.14489	-0.21671
$a = 0.5$, $k_e = 0.2$, $e_1 = 0.5$ and $\Lambda = -0.02$				$a = 0.5$, $k_e = 0.2$, $e_1 = -0.5$ and $\Lambda = -0.02$			
q_e	D_d	δ_s	δ	q_e	D_d	δ_s	δ
0.1	0.98554	0.02905	-0.14347	0.1	0.98085	0.03853	-0.18094
0.3	0.98463	0.03089	-0.15216	0.3	0.97905	0.04218	-0.19168
0.5	0.98234	0.03553	-0.17084	0.5	0.97385	0.05269	-0.21553
0.7	0.97678	0.04676	-0.20315	0.6	0.96794	0.06465	-0.23448
0.9	0.95385	0.09315	-0.26160	0.7	0.95385	0.09311	-0.26160
$a = 0.5$, $q_e = 0.2$, $e_1 = 0.5$ and $\Lambda = -0.02$				$a = 0.5$, $q_e = 0.2$, $e_1 = -0.5$ and $\Lambda = -0.02$			
k_e	D_d	δ_s	δ	k_e	D_d	δ_s	δ
0.2	0.98522	0.02971	-0.14668	0.1	0.98144	0.03734	-0.17709
0.4	0.98744	0.02523	-0.12235	0.2	0.97905	0.03981	-0.19168
0.6	0.98984	0.02039	-0.08735	0.3	0.97772	0.04497	-0.19875
0.8	0.99189	0.01627	-0.04641	0.4	0.97251	0.05541	-0.22044
1.0	0.99349	0.01305	-0.00304	0.5	0.95846	0.08381	-0.25466
$a = 0.5$, $q_e = k_e = 0.2$ and $\Lambda = -0.02$				$a = 0.5$, $q_e = k_e = 0.2$ and $\Lambda = -0.02$			
e_1	D_d	δ_s	δ	e_1	D_d	δ_s	δ
0.01	0.98318	0.03382	-0.16441	-0.01	0.98309	0.03402	-0.16517
0.4	0.98485	0.03046	-0.15017	-0.4	0.98089	0.03845	-0.18068
0.8	0.98621	0.02772	-0.13659	-0.8	0.97781	0.04468	-0.19818
1.2	0.98731	0.02548	-0.12389	-1.2	0.97324	0.05392	-0.21780
1.6	0.98824	0.02362	-0.11194	-1.6	0.96555	0.06951	-0.24055
$a = 0.5$, $q_e = k_e = 0.2$ and $e_1 = 0.5$				$a = 0.5$, $q_e = k_e = 0.2$ and $e_1 = -0.5$			
Λ	D_d	δ_s	δ	Λ	D_d	δ_s	δ
-0.01	0.98740	0.02530	-0.08111	-0.01	0.98281	0.03456	-0.12744
-0.03	0.98522	0.03212	-0.19965	-0.02	0.97905	0.03981	-0.19168
-0.05	0.98403	0.03396	-0.28099	-0.03	0.97870	0.04289	-0.23198
-0.07	0.98312	0.03395	-0.34143	-0.04	0.97782	0.04467	-0.27155
-0.09	0.98352	0.03314	-0.38868	-0.05	0.97735	0.04564	-0.30544

is estimated to be $\theta_0 = 50^\circ$ in the Sgr A*. As is seen from this table, the condition $\sqrt{3}/2 \leq D < 1$ is satisfied for the whole parameters for both cases I and II. The distortion δ_s is non-zero and becomes larger for larger rotation parameter, electric charge and cosmological constant in both cases. Regarding to the electric dilation charge and e_1 parameter, δ_s increases as these two parameters decrease (increase) in case I (case II). The fractional deviation δ increases by increasing the rotation parameter. For case I, the range $0 < a < 0.4$ satisfies 1σ Keck bound, while the range $0 \leq a \leq 0.8$ satisfies 1σ VLTI bound. For case II, no values of the rotation parameter can satisfy 1σ Keck bound. Only the range $0 < a < 0.1$ satisfies 1σ VLTI bound. But all values of a satisfy both VLTI and Keck bounds within 2σ uncertainty. Regarding the electric charge, as is seen from the second row of table IV, the 1σ Keck bound is not satisfied for any values of the electric charge for case I. While VLTI measurements within the 1σ confidence interval, constraint $0 < q_e < 0.5$. For case II, 1σ bound is never satisfied, but the range $0 < q_e \leq 0.6$ ($0 < q_e < 0.7$) can satisfy 2σ confidence interval of Keck (VLTI) measurements. From third row of table IV, we see that in case I,

all values of the electric dilation parameter k_e satisfy 1σ VLTI bound, while according to Keck measurements, for $k_e > 0.2$ this constraint can be satisfied. In case II, only 2σ Keck (VLTI) bound is satisfied in the range $0 < k_e \leq 0.45$ ($0 < k_e \leq 0.5$). According to forth row of table IV, in case I, 1σ VLTI bound is satisfied for all e_1 , while $e_1 \geq 0.8$ is the allowed range of this parameter to satisfy 1σ keck bound. For case II, only 1σ VLTI bound is satisfied in the range $-0.15 < e_1 < 0$, while 2σ Keck (VLTI) bound can be satisfied in the range $-1.6 < e_1 < 0$ ($-1.8 \leq e_1 < 0$). Regarding the cosmological constant, the range $-0.017 < \Lambda < 0$ ($-0.024 < \Lambda < 0$) satisfies 1σ Keck (VLTI) bound in case I. According to our analysis, for $\Lambda \leq -0.043$, the fractional deviation δ is beyond Keck/VLTI bound. For case II, the allowed range of Λ is $(-0.012, 0)$ for 1σ Keck bound and $(-0.017, 0)$ for 1σ VLTI bound. Our findings show that for $\Lambda \leq -0.04$, the fractional deviation δ is located outside Keck/VLTI measurements.

Table V shows the allowed regions of BH parameters for both cases for which the resulting shadow diameter is consistent with EHT data of M87*/SgrA* within $1\sigma/2\sigma$ uncertainty. As we see, for no values of the rotation parameter, electric charge and electric dilation parameter, d_{sh} is not in agreement with observations for M87* within 1σ uncertainty. Only for case I and in the range $2.5 < e_1 < 24$ or $-0.01 \leq \Lambda < 0$, a rotating BH located in a weak electric field has a compatible shadow with EHT data of M87* within 1σ uncertainty. But for given regions of parameters, the resulting shadow is located in 1σ confidence region of Sgr A* data for both cases I and II. So SgrA* black hole can be a suitable model for Kerr-Newman BHs in WCT.

TABLE V: Constraints on BH parameters for the two cases, Set by the EHT results.

Case	M87*		Sgr A*	
	$q_e = k_e = 0.2, e_1 = 0.5$ and $\Lambda = -0.02$		$q_e = k_e = 0.2, e_1 = -0.5$ and $\Lambda = -0.02$	
	1σ	2σ	σ	2σ
I	--	$a \in [0, 1.0)$	$a \in [0, 1.0)$	--
II	--	$a \in [0, 0.8)$	$a \in [0, 0.8)$	--
Case	$a = 0.5, k_e = 0.2, e_1 = 0.5$ and $\Lambda = -0.02$		$a = 0.5, k_e = 0.2, e_1 = -0.5$ and $\Lambda = -0.02$	
	1σ	2σ	σ	2σ
	I	--	$q_e \in [0, 0.82]$	$q_e \in [0, 0.85]$
II	--	$q_e \in [0, 0.6]$	$q_e \in [0, 0.64]$	$q_e \in (0.64, 0.7]$
Case	$a = 0.5, q_e = 0.2, e_1 = 0.5$ and $\Lambda = -0.02$		$a = 0.5, q_e = 0.2, e_1 = -0.5$ and $\Lambda = -0.02$	
	1σ	2σ	σ	2σ
	I	--	$k_e \in [0, 0.65]$	$k_e \in [0, 1.26]$
II	--	$k_e \in [0, 0.45]$	$k_e \in [0, 0.47]$	$k_e \in (0.47, 0.5]$
Case	$a = 0.5, q_e = k_e = 0.2$ and $\Lambda = -0.02$		$a = 0.5, q_e = k_e = 0.2$ and $\Lambda = -0.02$	
	1σ	2σ	σ	2σ
	I	$e_1 \in [2.5, 24)$	$e_1 \in [0, 2.5)$	$e_1 \in (0, 10)$
II	--	$e_1 \in [-1.48, 0)$	$e_1 \in (-1.28, 0)$	$e_1 \in [-2, -1.28]$
Case	$a = 0.5, q_e = k_e = 0.2$ and $e_1 = 0.5$		$a = 0.5, q_e = k_e = 0.2$ and $e_1 = -0.5$	
	1σ	2σ	σ	2σ
	I	$\Lambda \in [-0.011, 0)$	$\Lambda \in (-0.034, -0.011)$	$\Lambda \in [-0.034, 0)$
II	--	$\Lambda \in [-0.031, 0)$	$\Lambda \in [-0.029, 0)$	$\Lambda \in (-0.07, -0.029)$

V. CONCLUSION

The field of research in BH imaging and the optical appearance of black holes has experienced significant growth recently. Numerous studies have been conducted to explore how data from the Event Horizon Telescope (EHT) can be used to constrain various parameters of black holes. In this study, we specifically investigated Kerr-Newman black holes within the framework of WCT by examining their geometric and optical properties. Studying geometrical property, we found that there is an essential singularity at $r = 0$ and $\theta = \pi/2$ which is covered by an event horizon, confirming the existence of black holes in this theory of gravity. Then, we studied the optical features of black holes such as photon sphere radius and shadow size, and noticed that some constraints should be imposed on parameters of the model to have acceptable optical behavior. Studying the effect of parameters on the size and shape of the BH shadow, we found that the rotation parameter causes deformations to both of them. We also saw that the shape of the shadow depends on the inclination angle θ_0 of the far distant observer and is skewed as θ_0 increases. For the

case of $\theta_0 = 0$, the shadow is a round disk whereas at the equatorial plane ($\theta_0 = \pi/2$) it becomes most distorted. We examined the influence of electric charge on the BH shadow and observed that increasing this parameter leads to decreasing the shadow size. Regarding the electric dilation parameter, its effect on the radius of shadow was opposite (similar) to the electric charge in case I (case II). Investigating the cosmological constant effect, we found that $|\Lambda|$ decreases the shadow radii. We continued by calculating the energy emission rate and observed that the rotation parameter, electric charge, and $|\Lambda|$ decrease the emission rate, indicating that the evaporation process would be slow with an increase of these three parameters. Regarding the effect of the electric dilation parameter and e_1 on the energy emission rate, our findings showed that increasing k_e and $|e_1|$ makes increasing (decreasing) the emission rate in case I (case II).

Finally, we considered M87* BH and Sgr A* BH as models for Kerr-Newman BHs in WCT and imposed some constraints on the parameters of the model to have consistent results with observational data. Calculating the shadow diameter, we noticed that the resulting shadow of these BHs is not located within 1σ uncertainty of M87* data for no values of the rotation parameter, electric charge, and electric dilation parameter. While for given ranges of parameters, the resulting shadow was in agreement with observational data of Sgr A* in 1σ confidence region. This reveals the fact Sgr A* BH can be a suitable model for corresponding BHs. We also obtained the circularity deviation ΔC and axial ratio D_x and found that the constraint $\Delta C \lesssim 0.1$ is satisfied for the whole parameters of the model. While the condition $1 < D_x \lesssim 4/3$ imposes some constraints on k_e for case I and cosmological constants for both cases. Moreover, we computed the Schwarzschild shadow deviation (δ) by using measurements of M87* and SgrA*. According to our analysis, all values of the rotation parameter, electric dilation parameter, and parameter e_1 satisfy the 1σ bound of M87* measurements in case I, whereas in case II, 1σ bound can be satisfied only for special ranges of these parameters. Comparing the fraction deviation observable δ with values reported by SgrA* measurements, we found that resulting δ lies within both the VLTI and Keck bounds. For the case I, its δ is located in 1σ uncertainty, whereas for case II, δ lies in 2σ uncertainty.

Acknowledgments

SHH and KhJ thank Shiraz University Research Council. KhJ is grateful to the Iran Science Elites Federation for the financial support. SB is supported by JSPS Postdoctoral Fellowships for Research in Japan and KAKENHI Grant-in-Aid for Scientific Research No. JP21F21789.

[1] B. P. Abbott et al., *Phys. Rev. Lett.* **116** no. 6, (2016) 061102; R. Abbott et al., *Phys. Rev. D* **102** no. 4, (2020) 043015.
[2] K. Akiyama et al. *Astrophys. J. Lett.* **930** (2022) L12; K. Akiyama et al., *Astrophys. J. Lett.* **930** (2022) L13.
[3] K. Akiyama et al., *Astrophys. J. Lett.* **910**, L13 (2021); K. Akiyama et al., *Astrophys. J. Lett.* **910**, L12 (2021).
[4] K. Jusufi, S. Kumar, M. Azreg-Aïnou, M. Jamil, Q. Wu, C. Bambi, *Eur. Phys. J. C* (2022) 82:633; C. Bambi and D. Stojkovic, *Universe* (2021) **7**:136; V. Patel, D. Tahelyani, A. B. Joshi, D. Dey, P. S. Joshi, *Eur. Phys. J. C* **82**, 798 (2022).
[5] H.-T. Wang, P.-C. Li, J.-L. Jiang, G.-W. Yuan, Y.-M. Hu, and Y.-Z. Fan, *Eur. Phys. J. C* **81**, 769 (2021).
[6] S. G. Ghosh, M. Afrin, *Astrophys. J.* **944**, 174 (2023).
[7] A. F. Zakharov, *Universe* **8**, no.3, 141 (2022).
[8] M. Zajacek, A. Tursunov, A. Eckart, S. Britzen, E. Hackmann, V. Karas, Z. Stuchlík, B. Czerny, and J. A. Zensus, *J. Phys. Conf. Ser.* **1258**, 012031 (2019).
[9] M. Zajacek, A. Tursunov, A. Eckart, and S. Britzen, *Mon. Not. Roy. Astron. Soc.* **480**, 4408 (2018).
[10] F. C. Adams, M. Mbonye and G. Laughlin, *Phys. Lett. B* **450**, 339 (1999).
[11] B. Nayak and M. Jamil, *Phys. Lett. B* **709**, 118 (2012).
[12] P. F. Gonzalez-Diaz and C. L. Siguenza, *Phys. Lett. B* **589**, 78 (2004).
[13] S. Vagnozzi et.al, *Class. Quantum Grav.* **40**, 165007 (2023).
[14] K. Jusufi, S. Capozziello, S. Bahamonde, M. Jamil, *Eur. Phys. J. C* **82**, 1018 (2022); M. Ghasemi-Nodehi, M. Azreg-Aïnou, K. Jusufi, M. Jamil, *Phys. Rev. D* **102**, 104032 (2020); Y. Meng, X-M. Kuang, X-J. Wang, J-P. Wu, *Phys. Lett. B* **841** (2023) 137940; K. Jusufi, M. Azreg-Aïnou, M. Jamil, S-W Wei, Q. Wu, A. Wang, *Phys. Rev. D* **103**, 024013 (2021); C. Liu, T. Zhu, Q. Wu, K. Jusufi, M. Jamil, M. Azreg-Aïnou, A. Wang, *Phys. Rev. D* **101**, 084001 (2020); K. Jusufi, M. Jamil, H. Chakrabarty, Q. Wu, C. Bambi, A. Wang, *Phys. Rev. D* **101**, 044035 (2020); T. Zhu, Q. Wu, M. Jamil, K. Jusufi, *Phys. Rev. D* **100**, 044055 (2019); N. Parbin, D. J. Gogoi, U. D. Goswami, *Physics of the Dark Universe* **41** (2023) 101265; S. Haroon, M. Jamil, K. Jusufi, K. Lin, R. B. Mann, *Phys. Rev. D* **99**, 044015 (2019).
[15] R. Utiyama, *Phys. Rev.* **101**, 1597 (1956).
[16] F. W. Hehl, P. Von Der Heyde, G. D. Kerlick and J. M. Nester, *Rev. Mod. Phys.* **48**, 393 (1976).
[17] F. W. Hehl, J. D. McCrea, E. W. Mielke and Y. Ne'eman, *Phys. Rept.* **258**, 1 (1995).
[18] M. Blagojević and F. W. Hehl, “Gauge Theories of Gravitation : A Reader with Commentaries,” World Scientific (2013).

- [19] É. Cartan, “Sur une généralisation de la notion de courbure de Riemann et les espaces à torsion,” *Comptes Rendus, Ac. Sc. Paris* **174** (1922) 593–595.
- [20] É. Cartan, “Sur les variétés à connexion affine et la théorie de la relativité généralisée (première partie),” in *Annales scientifiques de l’École normale supérieure*, vol. 40, pp. 325–412. 1923.
- [21] A. Einstein, “Einheitliche Feldtheorie von Gravitation und Elektrizität,” *Sitzungsber. Preuss. Akad. Wiss* **22** (1925) 414.
- [22] A. Einstein, “Riemanngeometrie mit Aufrechterhaltung des Begriffes des Fern-Parallelismus,” *Sitzungsber. Preuss. Akad. Wiss* **17** (1928) 217.
- [23] A. Chatzistavrakidis, G. Karagiannis, and P. Schupp, *Eur. Phys. J. C* **80**, 1034 (2020).
- [24] R.-G. Cai, C. Fu, and W.-W. Yu, *Phys. Rev. D* **105**, 103520 (2022).
- [25] M. Li, Y. Tong, and D. Zhao, *Phys. Rev. D* **105**, 104002 (2022).
- [26] S. Bahamonde, K. F. Dialektopoulos, C. Escamilla-Rivera, G. Farrugia, V. Gakis, M. Hendry, M. Hohmann, J. Levi Said, J. Mifsud and E. Di Valentino, *Rept. Prog. Phys.* **86** (2023) no.2, 026901.
- [27] S. Bahamonde and J. G. Valcarcel, *JCAP* **09** (2020), 057.
- [28] S. Bahamonde and J. Gigante Valcarcel, *Eur. Phys. J. C* **81**, 495 (2021).
- [29] S. Bahamonde and J. G. Valcarcel, *JCAP* **01** (2022) no.01, 011.
- [30] S. Bahamonde, J. G. Valcarcel and L. Järv, *JCAP* **04** (2022) no.04, 011.
- [31] S. Bahamonde, and J. G. Valcarcel, *JCAP* **01**, 011 (2022).
- [32] S. Bahamonde and J. Gigante Valcarcel, *Phys. Rev. D* **108** (2023) no.4, 044037.
- [33] B. Carter, *Phys. Rev.* **174**, 1559 (1968).
- [34] Y. Decanini, A. Folacci, and B. Raffaelli, *Classical Quant. Grav.* **28**, 175021 (2011).
- [35] S. Chandrasekhar, *The Mathematical Theory of BHs* (Oxford University Press, New York, 1992).
- [36] S. E. Vazquez, and E. P. Esteban, *Nuovo Cim. B* **119**, 489 (2004).
- [37] X. H. Feng, and H. Lu, *Eur. Phys. J. C* **80**, 551 (2020).
- [38] B. Mashhoon, *Phys. Rev. D* **7**, 2807 (1973).
- [39] S. W. Wei, and Y. X. Liu, *J. Cosmol. Astropart. Phys.* **11**, 063 (2013).
- [40] K. Hioki, K.-i. Maeda, *Phys. Rev. D*, **80**, 024042 (2009).
- [41] R. Kumar, A. Kumar, S. G. Ghosh, *Astrophys. J.* **896**, 89 (2020)
- [42] K. Akiyama et al. (EHT Collaboration), *Astrophys. J.* **875**, L1 (2019).
- [43] C. Bambi, K. Freese, S. Vagnozzi, and L. Visinelli, *Phys. Rev. D* **100**, 044057 (2019).
- [44] K. Akiyama et al. (Event Horizon Telescope), *Astrophys. J. Lett.* **875**, L1 (2019).
- [45] K. Akiyama et al. (Event Horizon Telescope), *Astrophys. J. Lett.* **875**, L6 (2019).
- [46] K. Akiyama et al. (Event Horizon Telescope), *Astrophys. J. Lett.* **875**, L4 (2019).
- [47] R. Kumar and S. G. Ghosh, *Astrophys. J.* **892**, 78 (2020).
- [48] I. Banerjee, S. Chakraborty, and S. SenGupta, *Phys. Rev. D* **101**, 041301 (2020).
- [49] R. Craig Walker, P. E. Hardee, F. B. Davies, C. Ly, and W. Junor, *Astrophys. J.* **855**, 128 (2018).
- [50] K. Akiyama et al. (Event Horizon Telescope), *Astrophys. J. Lett.* **930**, L12 (2022).
- [51] M. Afrin, S. Vagnozzi, S. G. Ghosh, *Astrophys. J.* **944**, 149 (2023).
- [52] R. K. Walia, S. G. Ghosh, S. D. Maharaj, *Astrophys. J.* **939**, 77 (2022).
- [53] K. Akiyama et al. (Event Horizon Telescope), *Astrophys. J. Lett.*, **930**, L15 (2022).
- [54] S.Ul Islam, J. Kumar, R. K. Walia, S. G. Ghosh, *ApJ* **943**, 22 (2023).